UNIVERSITY OF CALIFORNIA, SAN DIEGO

Focused Helium Beam Irradiated Josephson Junctions

A dissertation submitted in partial satisfaction of the
requirements for the degree
Doctor of Philosophy

in

Physics

by

Ethan Y. Cho

Committee in charge:

Professor Robert C. Dynes, Chair
Professor Brian Maple
Professor Oleg Shpyrko
Professor Jan Talbot
Professor Charles Tu

2016

The dissertation of Ethan Y. Cho is approved, and it is acceptable in quality and form for publication on microfilm:

_____

_____

_____

_____

_____

Chair

University of California, San Diego

2016

EPIGRAPH

Everything takes longer than you think.

Be careful with what you wish for.
—Robert C. Dynes

TABLE OF CONTENTS

LIST OF FIGURES

ACKNOWLEDGEMENTS

I gratefully thank my adviser, Bob Dynes, who taught me condensed matter physics, along with the attitude and mindset to be a experimental physicist. Through his wit and wisdom, he showed me the pride and responsibilities of a great scientist. You will continue to be my role model for life.

I am very lucky to have a second "adviser," Shane Cybart, who guided me through my years as a graduate student. Your advice extend well beyond lab related events. You are an adviser, a lab mate, a scientist, lab manager, and above all, a friend to me.

My first two lab mates–Peter and Travis, together we moved and rebuilt Bob's old lab. I learned all basic construction tools and techniques during that time, especially Travis, from painting walls to name of different tools. As the only other graduate student in the lab, Travis, you and I shared many crazy lab experiences together, especially those late nights in the cleanroom or machine shop and early mornings at SPAWAR. Peter, our one and only postdoc, showed us different skills from ebeam lithography to Labview programming to sailing–these are the things I will remember. I cherish your friendship and thank you for all the things you have shown me.

Our lab has had many talented undergraduate students throughout the years who helped me. Kirill, I had a great time with you building the cleanroom. Bjorn, you have great math and computer skills that has helped me with simulations and modeling. Meng, you are one of the most dedicated and patient students in our lab, and you had helped me with all of my major accomplishments. When I was in the hospital for a week, you stayed with me and supported me. I am forever grateful and cherish our memories together. Lance, thank you for helping me with all the machining that I don't enjoy doing. Yuchao, even though you are crazy, I want to thank you for helping me with many late night measurements and programming. Jens, you are the most independent student that I have met and an textbook engineer. The PCBs and probe that you had built helped in many experiments. I want extent my thanks to Ashley who agreed to take on the incredible task of proofreading my thesis making it readable. Even though you are the most recent student, your dedication

and organization made you stand out from most of the students that we had.

I like to thank all of my collaborators: Adam at Oak Ridge National Lab, Chuong at Zeiss, and Doug and Kevin from Tristan Technologies that helped me with fabrication and measurements.

I also want to thank all of the physics department staffmembers Hilari, Patti, Sharmila, and Cathy, who kept me on track to meet the department requirements and deadlines. To Lester and Dirk, thank you for helping us building our lab so quickly and tolerating our wild actions throughout the years. Brandan and Kevin, thank you for helping me with all the data management and network problems I had over the years. Thank you Brad, you made everything very easy to understand while learning how to use all the tools in the machine shop and coming up with very creative ways of making the odd parts to fit our experiments. To George and Mike from the electronics shop, thank you for fixing whenever I had trouble with our electronics; you can always fix them even though the equipment were very ancient.

To my roommates, thank you for all the daily supportive conversations. Hsi-Ming Chang, not only have you taught me part of the field theory but also the advice for writing my thesis. Jhih-Shen Wu, thank you for taking your time to show me how to fit the energy gap temperature dependence and noise rounded current-voltage characteristics, even in you busiest moments.

Thank you, my wonderful sister who helped me with my fabrication without knowing any background of in lithography, and looked after me after I got out of the hospital. Lastly, I thank my parents who provided me with the environment to explore my interest and fully supported what I chose.

Chapter 3, in part, has been submitted for publication of the material as it may appear in *Nature Nanotechnology*, 2015, S. A. Cybart, E. Y. Cho, T. J. Wong, B. H. Wehlin, M. K. Ma, C. Huynh, and R. C. Dynes, Nature Publishing Group, 2015. The dissertation author was the primary investigator and author of this paper.

Chapter 4, in part, has been submitted for publication of the material as it may appear in *Microscopy and Microanalysis*, 2015, E. Y. Cho, Meng K. Ma, Chuong Huynh, R. C. Dynes, and Shane A. Cybart., Microscopy and Microanalysis, 2015. The dissertation author was the primary investigator and author of this paper.

Chapter 6, in part, has been submitted for publication of the material as it may appear in *Applied Physics Letters*, 2015, E. Y. Cho, M. K. Ma, C. Huynh, K. Pratt, D. N. Paulson, V. N. Glyantsev, R. C. Dynes, and S. A. Cybart, American Institute of Physics, 2015. The dissertation author was the primary investigator and author of this paper.

VITA

2009	B. S. in Physics, National Tsing Hua University, Taiwan
2016	Ph. D. in Physics, University of California, San Diego

PUBLICATIONS

S. A. Cybart, E. Y. Cho, T. J. Wong, B. H. Wehlin, M. K. Ma, C. Huynh, and R. C. Dynes, "Nano Josephson superconducting tunnel junctions in $YBa_2Cu_3O_{7-\delta}$ directly patterned with a focused helium ion beam", *Nature Nanotechnology*, 10(7), 598-602, June, 2015.

E. Y. Cho, M. K. Ma, C. Huynh, K. Pratt, D. N. Paulson, V. N. Glyantsev, R. C. Dynes, and S. A. Cybart, "$YBa_2Cu_3O_{7-\delta}$ superconducting quantum interference devices with metallic to insulating barriers written with a focused helium ion beam" *Applied Physics Letters* , 106(25), June, 2015.

S. A. Cybart, E. Y. Cho, T.J. Wong, V. N. Glyantsev, J. U. Huh, C. S. Yung, B. H. Moeckly, J. W. Beeman, E. Ulin–Avila, S. M. Wu, and R. C. Dynes, "Large voltage modulation in magnetic field sensors from two-dimensional arrays of Y-Ba-Cu-O nano Josephson junctions", *Applied Physics Letters*, 104(6), 2014.

E. Y. Cho, Meng K. Ma, Chuong Huynh, R. C. Dynes, and Shane A. Cybart. "Superconducting Nano Wire Circuits Fabricated using a Focused Helium Beam." Microscopy and Microanalysis 21, no. S3 (2015): 1997-1998.

S. A. Cybart, T. J. Wong, E. Y. Cho, J. W. Beeman, C. S. Yung, B. H. Moeckly, and R. C. Dynes, "Large scale two-dimensional arrays of magnesium diboride superconducting quantum interference devices", *Applied Physics Letters*, 104(18), 2014.

S. A. Cybart, P. X. T. Yen, E. Y. Cho, J. U. Huh, V. N. Glyantsev, C. S. Yung, B. H. Moeckly, J. W. Beeman, and R. C. Dynes, "Comparison of Y-Ba-Cu-O Films Irradiated with Helium and Neon Ions for the Fabrication of Josephson Devices", *IEEE Transactions on Applied Superconductivity*, 24(4), 2014.

ABSTRACT OF THE DISSERTATION

Focused Helium Beam Irradiated Josephson Junctions

by

Ethan Y. Cho
Doctor of Philosophy in Physics
University of California San Diego, 2016
Professor Robert C. Dynes, Chair

In this thesis, I studied the superconductor-insulator transition in thin film planar $YBa_2Cu_3O_{7-\delta}$ (YBCO) Josephson junctions with focused helium ion beams (FHB). Josephson junctions, patterned by a direct-write focused helium beam with a beam size of 500 pm, have a barrier width on the order of the quasiparticle tunneling length. By increasing the barrier strength with an irradiation dose that creates disorder in the material, the junction transitions continuously from a superconductor-normal metal-superconductor (SNS) to superconductor-insulator-superconductor (SIS). As described in model by Blonder, Tinkham, and Klapwijk (BTK), the transport mechanism shifts from Andreev reflection to tunneling. The product of critical current (I_C) and normal state resistance (R_N) is larger as a result of the higher resistance of the junction. Using high resistance SIS junctions, we measured the dynamic conductance of YBCO-YBCO junctions in the conduction plane. The peak of the dynamic conductance agrees with the reported values of the energy gap in the literature. In addition, the temperature dependence of the dynamic conductance peak fitted well with the temperature dependence of the energy gap in the Bardeen-Cooper-Scherifer (BCS) theory.

In the view of fabrication technology, an FHB can be used as a lithography

tool to pattern circuits. By applying higher irradiation dose, insulating barriers were created, defining the current paths and junction widths. Nano-scale features, which were difficult if not impossible with previous processing techniques, were directly written with an FHB. The smallest feature made with direct patterning with an FHB is 20 nm wide junction. Also I observed hysteretic current-voltage characteristics, from junctions with the Stewart-McCumber parameter β_C greater than 1. Nanopatterning with an FHB allows control over junction parameters of I_C, R_N, $I_C R_N$, and β_C that extended the parameter space of the junctions. With nanojunctions, superconducting electronics could be made with very high normal state resistance reaching several hundred ohms and be impedance matched with semiconductor electronics.

High-transition temperature superconductors have order parameters with some d-wave symmetry. I observed angular variation in I_C, R_N, and $I_C R_N$ of junctions in different orientations that have a similar pattern to the d-wave pattern. This experiment was conducted with YBCO-YBCO junctions, as opposed to different material interfaces that do not lie in the conduction plane. Junctions in certain directions exhibit $I_C R_N$ over 1 mV.

I also made superconducting quantum interference devices (SQUIDs) of FHB SIS and SNS junctions. A single SIS SQUID exhibits voltage modulation of 200 μV at 4 K. The SNS SQUID at 68 K has a flux noise of 10 $\mu\Phi_0/\mathrm{Hz}^{-1/2}$ in white noise range and 20 $\mu\Phi_0/\mathrm{Hz}^{-1/2}$ at 1 Hz, on par with the current state-of-the-art HTS SQUID in the white noise range and out performs it below 10 Hz. For most biomedical imagining applications, the signals below 10 Hz suggest HTS SQUID sensors could be an improvement to current technologies.

Lastly, 1D arrays of long Josephson junctions could potentially be an alternative for applications that require large dynamic range. For a 10 micron-wide, six hundred series junctions array, the voltage modulation was 23 mV, appearing linear over 12 mV and 30 μT, with a slope or transfer function of 500 V/T. As the junctions widens, the V–B skews more. In principle, with proper design of the junction width, the transfer function can be much larger.

Chapter 1

Josephson Junctions

1.1 Introduction to Josephson junctions

Superconductors have unique properties such as zero DC resistance, Meissner effect (magnetic flux exclusion) and quantized magnetic flux in a loop, that have potential applications. The superconducting electronics based on these unique properties are currently used or show promising potential for new applications. Some of the applications include non-invasive biomedical detection and imaging, specifically magnetoencephalography (MEG) [1, 2, 3] and magnetocardiography (MCG) [4, 5, 6, 7]. Additionally, superconducting electronics are of great interest for many applications in the field of communication [8, 9, 10], digital circuits [11, 12, 13, 14, 15, 16] and geoimaging [17]. Furthermore, these electronics are also used as an international voltage standard at the National Institute of Standards and Technology [18, 19]. In astrophysics, a single photon detector, a bolometers that uses the superconducting transition, is often used in telescopes or deep space probes [20, 21]. Since superconductivity is a macroscopic quantum mechanical phenomenon, it is also considered as one of the potential pathways to quantum computation [22, 23, 24, 25, 26, 27, 28, 29]. Studying the different physical effects and device functions will provide a better understanding of the physics of superconductivity.

The fundamental element in most superconducting electronics is the Josephson junction. It was first predicted by Brian Josephson in 1962 [30] when he considered the Cooper pair tunneling term, which was originally left out in the formulation of

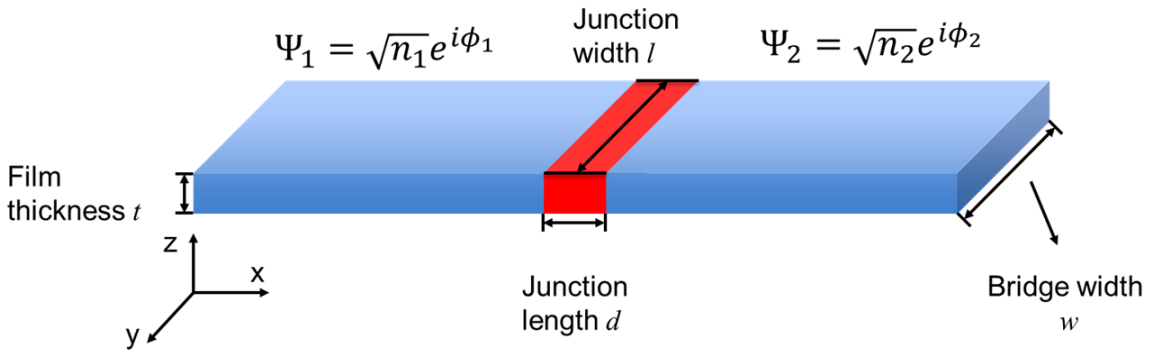

Figure 1.1: A schematic of Josephson junction. The blue blocks represent superconducting electrodes and the red block is the junction barrier.

tunneling Hamiltonian in the BCS theory [31]. He proposed two equations to describe the Cooper pairs tunneling through a thin insulating barrier separating two superconductors. The barrier/weak link can be either an insulator (SIS) or a metal/weak superconductor (SNS). Figure 1.1 shows a schematic of a Josephson junction.

To derive the Josephson equations in the absence of a magnetic field, consider the coupling between the two superconducting electrode wavefunctions ($\Psi = \sqrt{n}e^{i\phi}$), where n is the pair density, and ϕ is the superconducting phase. If K is the coupling constant that couples the two superconductors across the barrier, then the coupled Schrodinger equations for a Josephson junction are

$$\begin{cases} i\hbar\dfrac{\partial\Psi_1}{\partial t} = E_1\Psi_1 + K\Psi_2 \\ i\hbar\dfrac{\partial\Psi_2}{\partial t} = E_2\Psi_1 + K\Psi_1. \end{cases} \tag{1.1}$$

Substitute $\Psi = \sqrt{n}e^{i\phi}$ into Eq. (1.1)

$$\begin{cases} \dfrac{\dot{n}_1}{2\sqrt{n_1}}e^{i\phi_1} + i\sqrt{n_1}e^{i\phi_1}\dot{\phi}_1 = -\dfrac{i}{\hbar}\left[E_1\sqrt{n_1}e^{i\phi_1} + K\sqrt{n_2}e^{i\phi_2}\right] \\ \dfrac{\dot{n}_2}{2\sqrt{n_2}}e^{i\phi_2} + i\sqrt{n_2}e^{i\phi_2}\dot{\phi}_2 = -\dfrac{i}{\hbar}\left[E_2\sqrt{n_2}e^{i\phi_2} + K\sqrt{n_1}e^{i\phi_1}\right]. \end{cases} \tag{1.2}$$

Taking the real part of Eq. (1.2)

$$\begin{cases} \dfrac{\dot{n}_1}{2\sqrt{n_1}} = \dfrac{K}{\hbar}\sqrt{n_2}\sin(\phi_2 - \phi_1) \\ \dfrac{\dot{n}_2}{2\sqrt{n_2}} = \dfrac{K}{\hbar}\sqrt{n_1}\sin(\phi_1 - \phi_2). \end{cases} \tag{1.3}$$

Assuming the two superconducting electrodes are the same gives

$$\dot{n} = 2\frac{K}{\hbar} n \sin(\phi_2 - \phi_1). \tag{1.4}$$

Consider a unit volume. Then, the DC Josephson equation which states that a supercurrent I can flow in the absence of a voltage, up to a critical current I_{C}, becomes

$$I = I_{\mathrm{C}} \sin \Delta\phi \tag{1.5}$$

where $\Delta\phi = \phi_2 - \phi_1$ is the phase difference between the two superconducting order parameters of the electrodes. The $\Delta\phi$ across the junction is assumed as a constant in the y direction. In the presence of an external magnetic field, the gauge invariant phase has to be considered and the Josephson equation in Eq. (1.5) is now

$$I = I_{\mathrm{C}} \sin \gamma, \tag{1.6}$$

where

$$\gamma = \Delta\phi - \int \boldsymbol{A} \cdot d\boldsymbol{s} \tag{1.7}$$

is the gauge invariant phase and $\boldsymbol{A}$ is the vector potential. Figure 1.2 shows the current distribution in the junction with different applied magnetic fields (field is applied perpendicular to the page). When the applied magnetic field multiplied by an area A of the junction is equivalent to an integer multiple of a flux quantum (Φ_0), then the circulating current forms vortices.

The second Josephson equation can be obtained by taking the imaginary part of Eq. (1.2). Here E_1 is generally not identical to E_2 as we can assume that $E_1 - E_2$ represents the voltage across the junction.

$$\begin{cases} \sqrt{n_1}\dot{\phi}_1 = -\dfrac{i}{\hbar}\left[E_1\sqrt{n_1} + K\sqrt{n_2}\cos(\phi_2 - \phi_1)\right] \\ \sqrt{n_2}\dot{\phi}_2 = -\dfrac{i}{\hbar}\left[E_2\sqrt{n_1} + K\sqrt{n_1}\cos(\phi_1 - \phi_2)\right]. \end{cases} \tag{1.8}$$

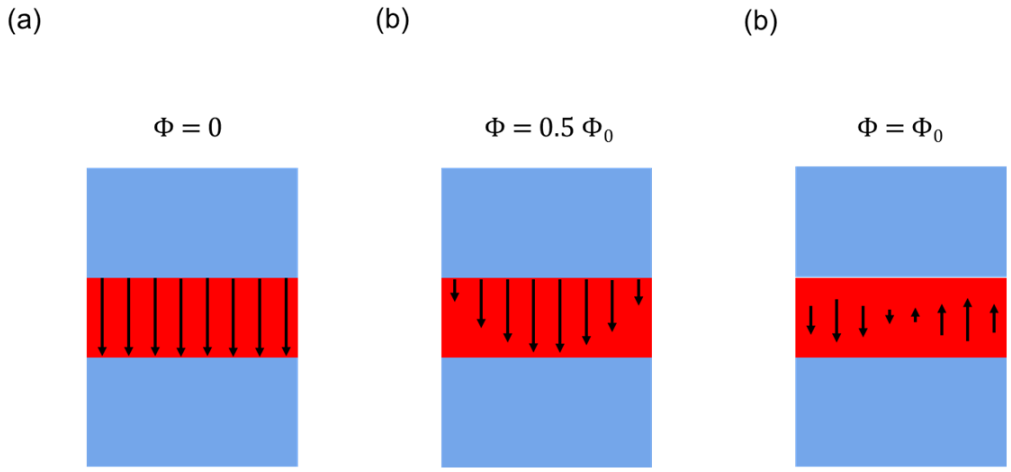

Figure 1.2: Current distribution in a short Josephson junction, where short will be defined later, with external applied magnetic field equal to (a) zero, (b) half flux quantum, and (c) one flux quantum.

Using the same assumption as previously for the real part and subtracting the two equations, we get

$$\frac{d}{dt}(\phi_2 - \phi_1) = \frac{E_2 - E_1}{\hbar}. \tag{1.9}$$

Since a Cooper pair carries a charge of $2e$, the voltage across the junction is

$$V = \frac{\hbar}{2e}\frac{d\Delta\phi}{dt} \tag{1.10}$$

which is the AC time dependent (second) Josephson equation where $\Delta\phi = \phi_2 - \phi_1$. This second Josephson equation relates the time dependence of the phase difference to the voltage across the junction, the time averaged value of the $\Delta\dot{\phi}$ gives a DC voltage. Figure 1.3 demonstrates the current-voltage characteristic (I–V) of a typical Josephson junction that is described by the two equations 1.5 and 1.10. Although there was some controversy when Josephson first proposed his theory, it became widely accepted after John Rowell and Phil Anderson confirmed the modulation of the I_C in an externally applied magnetic field [32].

When a Josephson junction is driven by a DC and AC voltage source, there

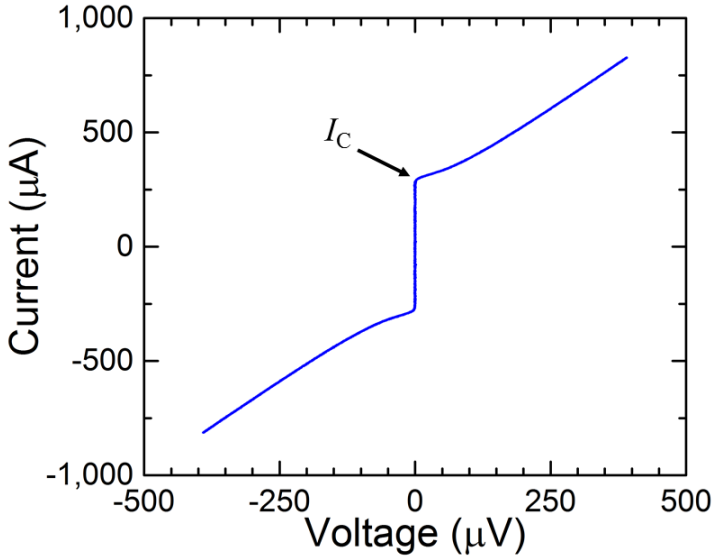

Figure 1.3: Current-voltage characteristics of a typical Josephson junction.

will be steps occurring in resonance at

$$V = n\frac{h\nu}{2e} \tag{1.11}$$

, where ν is the AC frequency. These steps were first observed by Shapiro and are called Shapiro steps [33]. Combining AC (1.10) and DC (1.5) Josephson equations we have

$$I(t) = I_C \sin\left[\int \frac{2eV(t')}{\hbar}dt' + \phi_0\right]. \tag{1.12}$$

By assuming $V(t) = V_0 + V_{AC}\cos\omega_{AC}t$, and using trigonometric identities and Bessel function relations Eq. (1.12) becomes

$$I(t) = I_C \sum_{n=-\infty}^{+\infty} (-1)^n J_n\left(\frac{2eV_{AC}}{\hbar\omega_{AC}}\right) \sin\left[(\omega - n\omega_{AC})t + \phi_0\right] \tag{1.13}$$

where J_n is the Bessel function of the first kind. Figure 1.4 shows a typical I–V for a Josephson junction exposed to a 12 GHz RF signal where the step height is determined by the Bessel function.

All the equations described above are under the assumption that the phase along the junction length is constant. However, when the junction length is longer

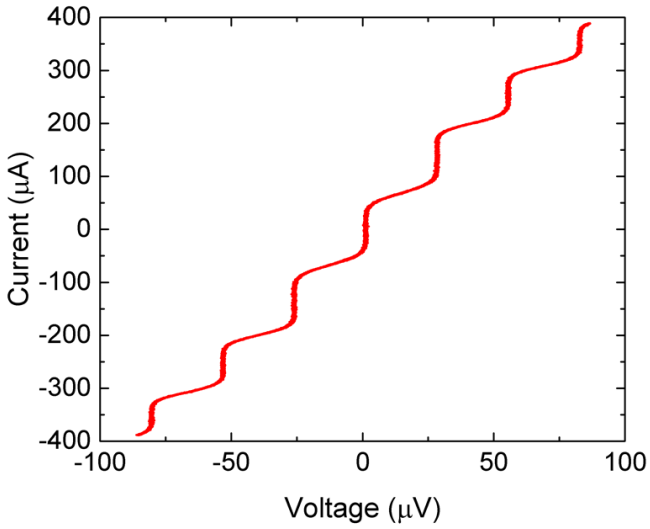

Figure 1.4: I–V of a Josephson junction irradiated with a 12 GHz radio frequency source demonstrating Shapiro steps.

than the Josephson penetration depth (λ_J), this assumption is no longer valid. To derive λ_J and the spatial dependence of the phase, consider a surface in the cross section of the junction as illustrated in Fig. 1.5. From Faraday's Law in the z-direction,

$$\oint \boldsymbol{E} \cdot d\boldsymbol{s} = w\frac{\partial E_x}{\partial z}dz = -\frac{\partial \Phi}{\partial t} = -\frac{\partial B_y}{\partial t}(2\lambda + w)dz. \tag{1.14}$$

By taking $\dfrac{\partial}{\partial z}$ on both sides, we get

$$\frac{\partial^2 E_x}{\partial z^2} = -\left(\frac{2\lambda + w}{w}\right)\frac{\partial^2 B_y}{\partial t \partial z}. \tag{1.15}$$

Similarly, for the y-direction,

$$\frac{\partial^2 E_x}{\partial y^2} = \left(\frac{2\lambda + w}{w}\right)\frac{\partial^2 B_z}{\partial t \partial y}. \tag{1.16}$$

From the Ampere-Maxwell equation in the x-direction,

$$\frac{1}{\mu}\left(\frac{\partial B_z}{\partial y} - \frac{\partial B_y}{\partial z}\right) = \frac{J_x}{\partial t} + \frac{1}{\epsilon}\frac{\partial E_x}{\partial t} \tag{1.17}$$

Then by taking $\dfrac{\partial}{\partial t}$ on both sides and using Eq. (1.15) and Eq. (1.16), we have

$$\left(\frac{\partial^2}{\partial y^2} + \frac{\partial^2}{\partial z^2} - \frac{1}{v^2}\frac{\partial^2}{\partial t^2}\right)E_x = \frac{1}{\epsilon v^2}\frac{\partial J_x}{\partial t}, \tag{1.18}$$

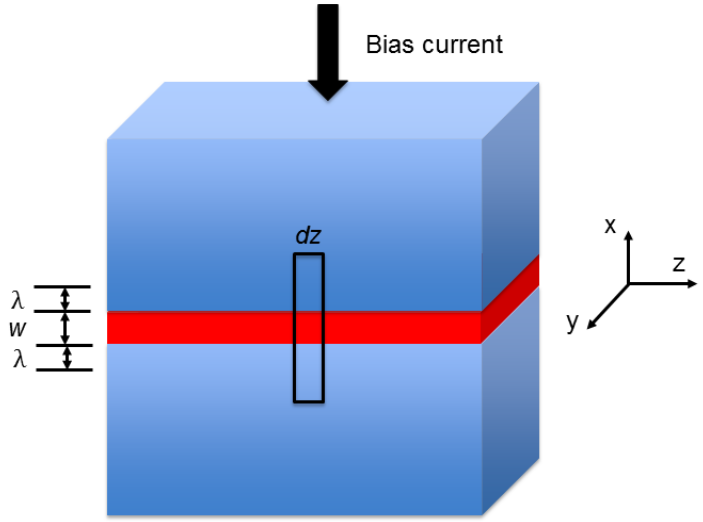

Figure 1.5: A cross-sectional surface in a Josephson junction considered in the derivation.

where $v^2 = \dfrac{1}{\mu\epsilon}\dfrac{w}{2\lambda + w}$. Next, from Eq. (1.5) and Eq. (1.10), we have

$$\begin{cases} J_x = -J_{\mathrm{C}} \sin\gamma \\ \dfrac{\partial\phi}{\partial t} = \dfrac{2eV}{\hbar} = -\dfrac{2eE_x w}{\hbar}. \end{cases} \tag{1.19}$$

Substitute the above into Eq. (1.18) and finally we have

$$\left(\frac{\partial^2}{\partial y^2} + \frac{\partial^2}{\partial z^2} - \frac{1}{v^2}\frac{\partial^2}{\partial t^2}\right)\gamma = \frac{\sin\gamma}{\lambda_{\mathrm{J}}^2}, \tag{1.20}$$

where

$$\lambda_{\mathrm{J}}^2 = \frac{\hbar}{2eJ_{\mathrm{C}}\mu_0(2\lambda + w)}. \tag{1.21}$$

The physical interpretation of this length is that the magnetic field penetrates the junction to λ_{J} just as λ does in bulk material. When the length of the junction is much less than λ_{J}, the short junction limit, then the current is uniform in the junction (Fig. 1.6(a)). In the long junction limit, when $\lambda_{\mathrm{J}} << l$, current will be constricted along the edge of the junction to a length λ_{J} for a time independent solution. For a time-dependent solution, flux will be propagating through the junction, with the propagating vortices traveling along the junction normal to the current (Fig. 1.6(b)).

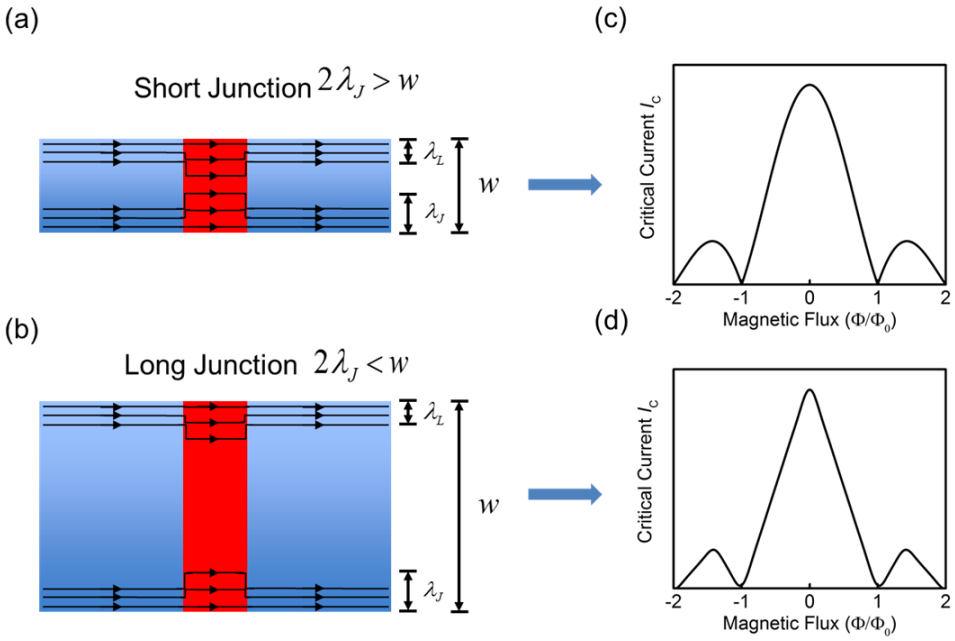

Figure 1.6: Current distribution in (a)(c) short and (b)(d) long junction with corresponding critical current magnetic field response.

Eq.(1.20) has the same form as the sine-Gordon equation for a series of coupled pendula.

From the time independent DC Josephson equation the critical current is a function of magnetic field. In figure 1.6(c) and (d), we show the corresponding critical current-magnetic field response ($I_C(B)$). For short junctions, the $I_C(B)$ is a sinc function

$$I_C(B) = \left| \frac{\sin(\frac{\pi\Phi}{\Phi_0})}{\frac{\pi\Phi}{\Phi_0}} \right| = \left| \mathrm{sinc}(\frac{\pi\Phi}{\Phi_0}) \right| \tag{1.22}$$

where $\Phi = BA$ is the flux through the junction and $\Phi_0 = 2.07 \times 10^{-15}$Wb is the magnetic flux quanta. This is analogous to the Fraunhofer pattern in a single slit optical diffraction experiment. As the junction gets longer, and the current distribution is no longer uniform, $I_C(B)$ deviates from the Fraunhofer pattern. The $I_C(B)$ of long junctions eventually enter a regime of a multivalued function due to self-field effects [34].

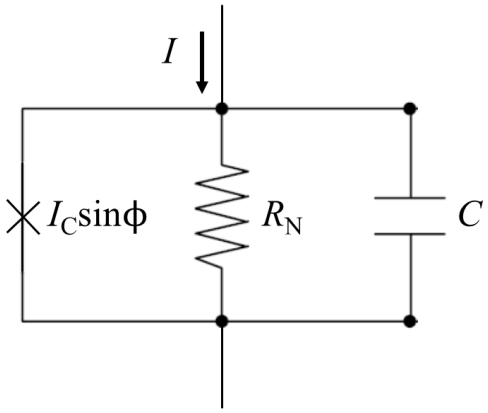

Figure 1.7: A circuit diagram of the resistively capacitively shunted Josephson junction model.

1.2 Resistively capacitively shunted junction model

In 1968 Stewart [35] and McCumber [36] independently developed an equivalent circuit model that describes the Josephson junction. The model they proposed later called the resistively capacitively shunted junction (RCSJ) model, which consists of a DC Josephson component in parallel with a resistor and a capacitor as illustrated in figure 1.7. The slope of the I–V curve of such a junction approaches a constant resistance at high bias, which is the resistance represented by the normal state resistance (R_{N}) in the RSCJ model. The current across the junction can be written as the sum of the currents through the three components.

$$I = I_{\mathrm{C}} \sin\phi + \frac{V}{R_{\mathrm{N}}} + C\frac{dV}{dt}. \tag{1.23}$$

By using Eq. (1.10) the above equation can be presented as a second order differential equation in phase

$$I = I_{\mathrm{C}} \sin\phi + \frac{\hbar}{2eR_N}\frac{d\phi}{dt} + \frac{\hbar C}{2e}\frac{d^2\phi}{dt^2} \tag{1.24}$$

or in dimensionless variables

$$I = I_{\mathrm{C}} \sin\phi + \frac{d\phi}{d\theta} + \beta_C\frac{d^2\phi}{d\theta^2} \tag{1.25}$$

where $\theta = \dfrac{2e}{\hbar} I_{\mathrm{C}} R_{\mathrm{N}} t$ and

$$\beta_C = \frac{2e}{\hbar} I_{\mathrm{C}} R_{\mathrm{N}}^2 C \tag{1.26}$$

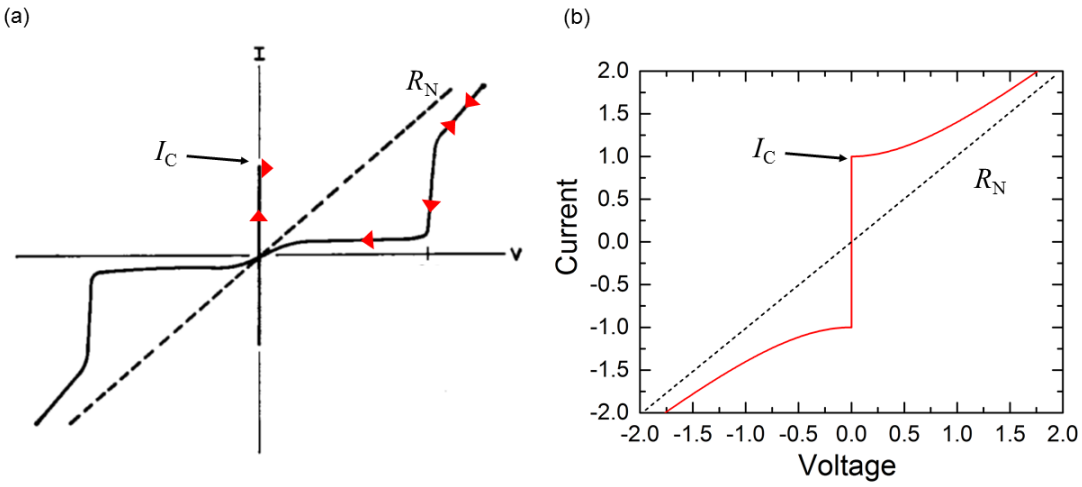

Figure 1.8: I–V of (a) an underdamped junction [37] and (b) an overdamped junction. At high bias the I–V approaches Ohm's law with slope R_N indicated in the figure as the dashed line. In (a) the red arrows show the re-entry voltage path different from the supercurrent.

is the Stewart-McCumber parameter Eq. (1.25) is the same as a driven damped pendulum. For an underdamped junction, where β_C is large ($beta_C >> 1$), the I–V is hysteretic (Fig. 1.8(a)) [37]. On the contrary, when β_C is small (overdamped case), there is no hysteresis in the I–V characteristics (Fig. 1.8(b)) and Eq. (1.25) becomes a first order differential equation with analytic solution

$$V = \begin{cases} 0 & I < I_C \\ I_C R_N \sqrt{\left(\frac{I}{I_C}\right)^2 - 1} & I > I_C. \end{cases} \tag{1.27}$$

The product of critical current and normal state resistance ($I_C R_N$) is usually used as the parameter to describe junction quality.

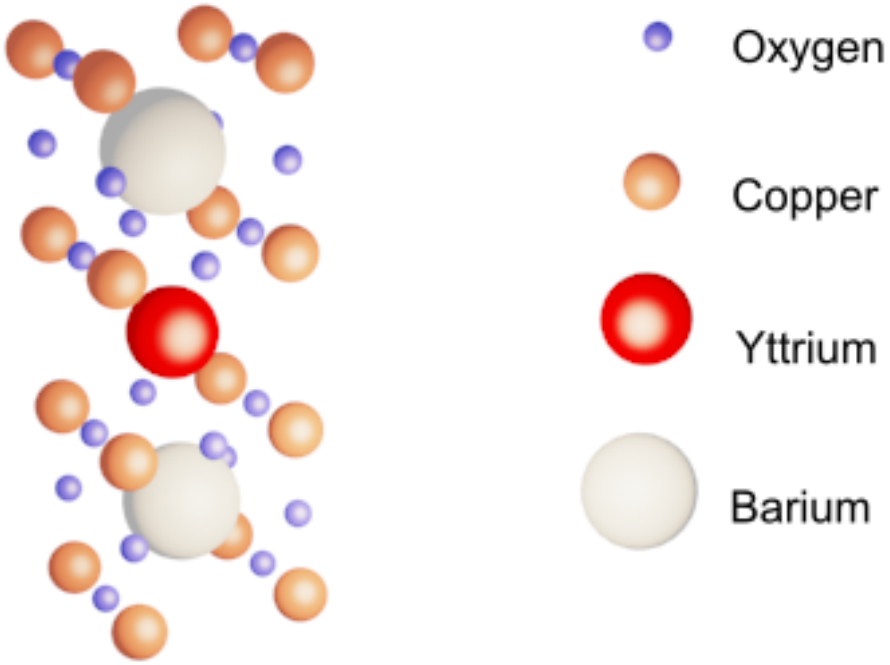

Figure 1.9: A 3D YBCO crystal unit cell model.

1.3 High transition temperature superconducting Josephson junctions

Just as scientists around the world thought the mystery of superconductivity had been solved and the highest T_C would not exceed 30 K according to BCS theory, a group of scientists at IBM Zurich discovered a ceramic that superconducted at 35 K [38]. Soon after, Paul Chu and his group discovered $YBa_2Cu_3O_{7\delta}$ (YBCO) [39], which superconducted at 93 K, which is well above the boiling point of liquid nitrogen (77 K). A huge family of cuprates was subsequently discovered by researchers around the world with T_Cs higher than 77 K. Scientists were ready and eager to transfer all the technologies developed from conventional superconductors or low temperature superconductor (LTS) to these high temperature superconductors (HTS). However, HTS materials have complex crystal structures. For example, YBCO is anisotropic in all directions, in both crystal structure and superconducting properties (Fig. 1.9).

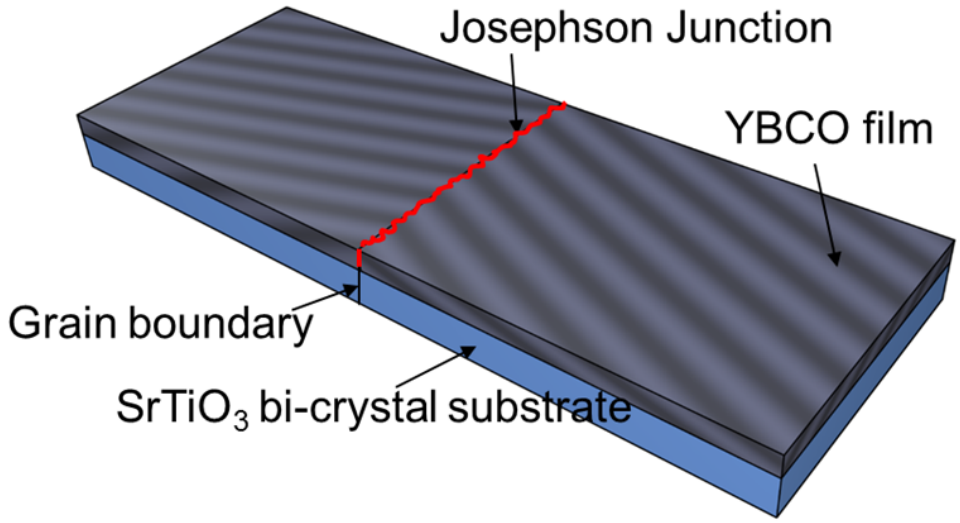

Figure 1.10: A bicrystal junction on $SrTiO_3$ substrate.

Not only is the coherence length ($\xi_{YBCO} \sim 2$ nm) much shorter than the conventional superconductors ($\xi_{Nb} \sim 50$ nm), but YBCO also has an orthorhombic unit cell and the ξ_c is estimated about an order of magnitude shorter in the c-axis than the ξ_{ab} in the ab-plane [40]. In addition, the order parameter in the HTS has a more complex, higher order d-wave and s-wave symmetry as opposed to only the s-wave in LTS. For a conventional superconductor, the electron density is on the order of $10^{23}/\text{cm}^3$ and the coherence length is approximately 50 nm; therefore, the number of electrons/pairs in a coherence volume $(50\text{ nm})^3$ is on the order of tens of millions. On the other hand, cuprate superconductors have an electron density only on the order of $10^{21}/\text{cm}^3$ and a coherence volume much smaller ($\sim 1\text{ nm}^3$), resulting only one or few electron pairs in a coherence volume. The electron-phonon interaction in the BCS theory that created the attractive retarded potential is not believed to be the coupling mechanism for HTS materials. However, the mechanism for the attractive potential in HTS is still unknown. To make matters even more complicated, high-quality films are c-axis oriented, which means the high conductivity path has to be along the ab-plane. These requirements complicated most of the technologies developed based on LTS, a multilayer technology. With the physics still unknown and difficult processing required,

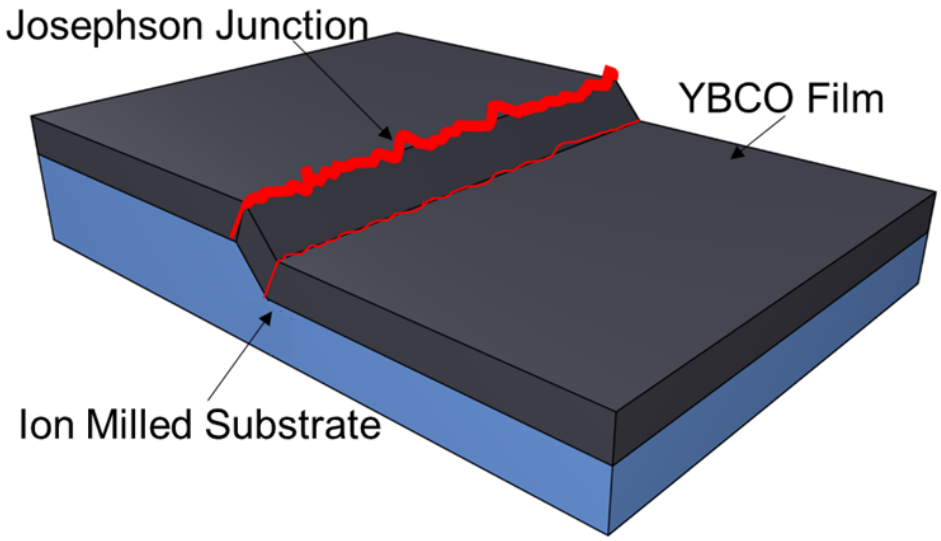

Figure 1.11: A schematic of a ramp edge junction.

applications of HTS materials did not advance as rapidly as everyone predicted and hoped. Nevertheless, progress has been made in both the growth of the material and the processing technique.

Early successful junctions were made on a bicrystal substrate. When YBCO films are grown over grain boundaries, junctions were formed directly on top of the boundary. As illustrated in figure 1.10 a junction is formed at the break of the grain boundary; however, the break on the substrate is a jagged line across the bridge. There is little control over the junction formation. As a result, some of the best junctions were grain boundary junctions but the variation between the junctions on a single chip was large compared with other types of junctions. For grain boundary junctions, the $I_C R_N$ products generally have a variation of 30% or more. Although it is simple to process and suitable for research, the lack of control of junctions and the confinement to the one-dimensional break limits the potential of this as a technology.

To tackle the limitation of grain boundary junctions, researchers developed artificial grain boundaries by ion milling a ramp on MgO substrates (Fig 1.11). With proper milling methods, it is possible to create a junction at the top of the ramp and have a smooth transition at the bottom. Therefore, junction placements could

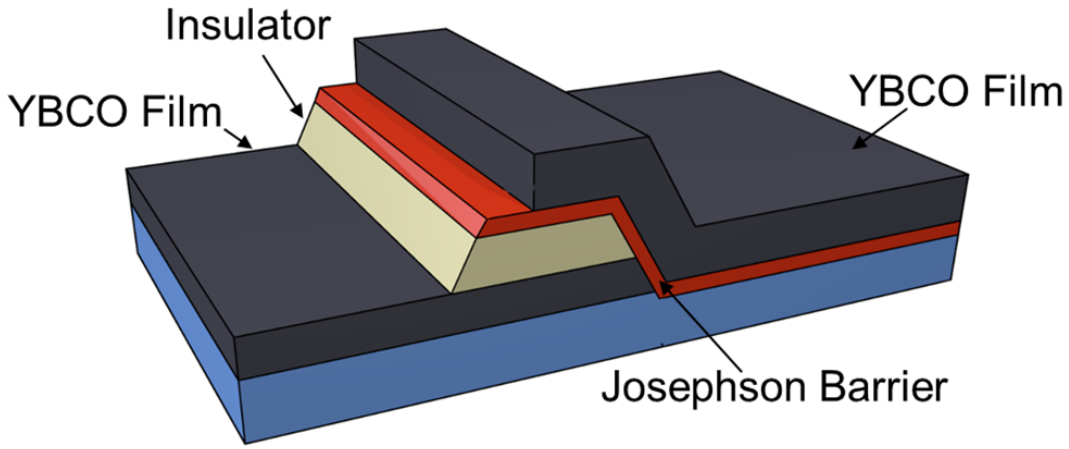

Figure 1.12: A schematic of a step edge junction.

be extended to two dimensions on the chip with two possible orientations. However, ramp junctions still use the same principle as grain boundary junctions in that the variation is still large and uncontrollable. The downsides of a MgO substrate include hydrophilic behavior, short lifetime, and limitations on the substrate size.

One of the most successful junction technologies is the step edge junction (Fig. 1.12). The technology matches the quality of the previous technologies but with much better control over the $I_C R_N$ product and the variation. However, the processing steps are a lot more complicated due to the multilayer process. In order to have high quality and stable YBCO after processing, the insulating layer and the barrier layer require multiple buffer layers. The substrate size is also still limited as the technologies described previously.

Finally, the masked ion/electron irradiated junction technology has perhaps the most potential [41, 42, 43, 44, 45]. This technology is different from the technologies mentioned above because junctions are created by the disorder caused by high energy ion/electron irradiation (Fig. 1.13) The principle of this technology is based on the fact the YBCO undergoes a superconductor-insulator transition as the disorder in the crystal increases. Therefore, the junction barrier can be "written" from the starting material, eliminating problems at the interface and resulting in better uniformity of $I_C R_N$. Since the junction direction and position are determined by

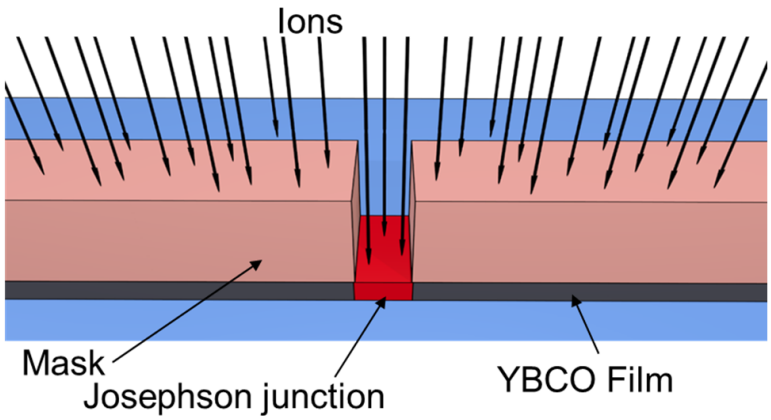

Figure 1.13: A schematic of an ion irradiated junction.

the mask, this technique is a 2D technology without any limitation on the junction direction and with much higher density than the others. It is scalable to wafer scale processes since there is no limitation on the substrate material [46]. The downside of this technology is that the $I_C R_N$ product is about an order of magnitude lower and that the fabrication of the mask is very difficult. The following chapters will discuss more about ion irradiation technology.

Chapter 2

Ion Irradiated Junctions

2.1 Superconductor-insulator transition

Superconductivity can be disrupted in two ways: phase decoherence or pair amplitude suppression [47]. Previous studies by Merchant *et al.* [48] have shown that phase decoherence broadens the superconducting transition width with respect to temperature. In [48], lead was quench condensed onto different substrates forming grains with different coupling constants between grains. Each grain is well defined by an individual superconducting wavefunction, each with its T_C of lead. However, the phase of each grain is unique; therefore, the whole film is in a phase fluctuating regime. This phase fluctuating regime results in the same onset temperature for each grain but the macroscopic film has a broadened transition width. For substantial grain-grain decoupling the resistive transition disappears. Figure 2.1 illustrates the transition width increases with weaker coupling between the grains.

On the other hand, in a study by Xiong *et al.* [49] it was shown that pair amplitude suppression does not change the transition width but does change T_C. The experiment was done by quench condensing multilayer stacks of Pb/Sn or Pb/Ge to form a completely amorphous lead film with grain sizes less than the coherence length. This resulted in no individual islands of lead with different superconducting phase. The pair amplitude in their experiment is controlled by the number of multilayer stacks or resultant resistance per square ($R/\square$). The results shown in figure 2.2 suggest as the pair amplitude is enhanced at lower $R/\square$, the T_C of the

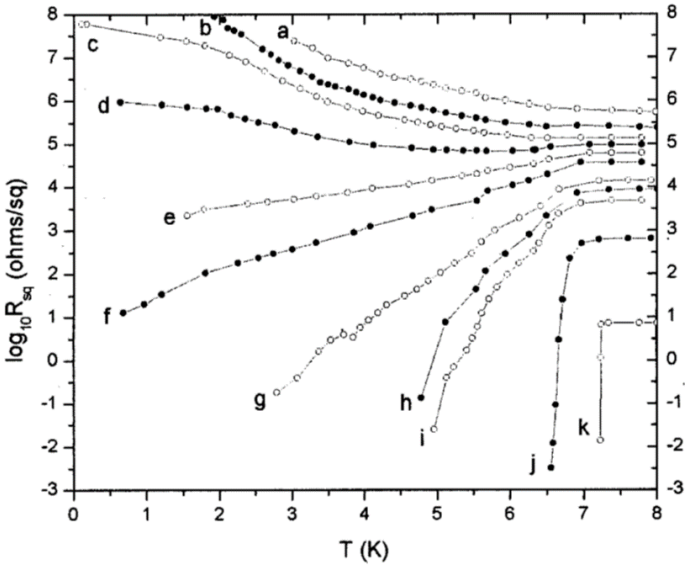

Figure 2.1: Sheet resistance versus temperature plot by Merchant *et al.*, showing superconducting transition narrows from (a) smaller to (k) larger grain size [48].

film approaches the bulk T_C. Since the phase remains coherent over the film, the T_C transition temperature width stays sharp and well defined for all thicknesses.

In high temperature superconductors, superconductivity can be disrupted with ion irradiation [50, 51, 52]. The disruption includes both phase decoherence and pair amplitude suppression. Although the previous experiments were done with a conventional superconductor, lead, the same principle described above can be applied to high temperature superconductors. The ion irradiation generates point defects in the HTS material, which increase the electron or hole scattering rate and the depletion of carriers. Therefore, the superconductor undergoes the superconductor-insulator transition. The nodes and opposite phases from the d-wave symmetry of HTS order parameter make the material more sensitive to disorder. Studies done by White *et al.* and Lang *et al.* [50, 51, 52] have shown the superconductor-insulator transition in YBCO films irradiated with different ion beams. Figure 2.3 shows YBCO films irradiated with different doses. As dosage increases, the resistivity of the films increases and the T_C decreases. At lighter doses, the primary disruption of superconductivity is by the suppression of the pair amplitude, where the transition width is still narrow.

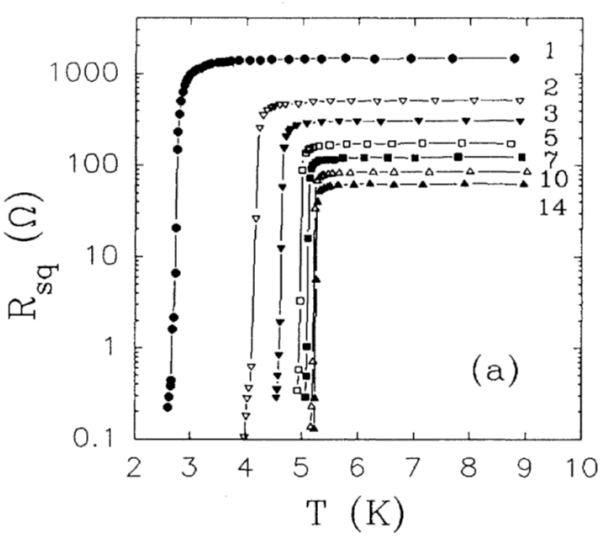

Figure 2.2: Sheet resistance versus temperature plot by Xiong *et al.*, shows the superconducting transition onset temperature increasing as the number of layers increases from 1 to 14 [49].

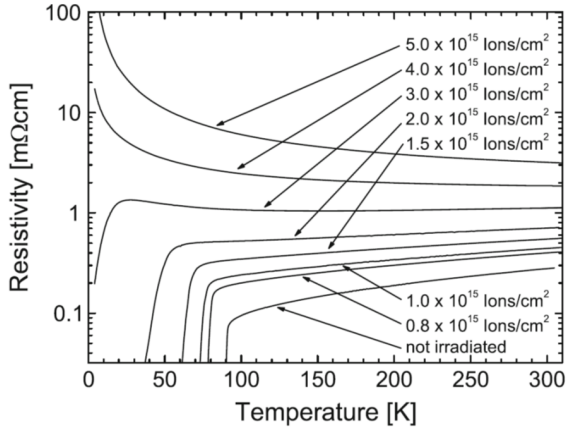

Figure 2.3: Resistivity versus temperature plot by Lang *et al.* showing superconducting transition for different ion irradiation doses. In this example, the material transitions to an insulator at a dose of 4×10^{15} ions/cm^2 [52].

As opposed to conventional superconductors, where T_C approaches a finite temperature when disordered, the superconductor-insulator transition in YBCO results from a radiation induced transition to insulator. Since the transition is continuous, it is possible to have barriers transitioning the full range of the transition without having to form interfaces with different materials.

2.2 Electrical properties of ion irradiated junctions

Using the superconductor-insulator transition of YBCO, researchers have demonstrated the modification of YBCO electrical properties on the nanoscale to create single junctions and Josephson junctions in large scale arrays [41, 46]. The fabrication of these devices involves multiple stages of processing. Each step requires extreme care during processing. Fortunately, all of the processes described above can be adopted from already available processing technologies within the semiconductor industry. Therefore, this ion damage technology has the potential to be easily scalable to large wafers. The first step is to use photolithography and Ar^+ ion milling to define the electrodes on the micron length scale. The second step is to deposit an e-beam resist-Ge-photoresist trilayer mask structure for e-beam lithography and then a two-step reactive ion etch (RIE) to create an ion mask with nanochannels to define where the junctions will be. The ion implantation step to create the junctions requires high enough energy ions to penetrate YBCO films creating disorder while being buried in the covering resist to protect the remainder of the YBCO films. The ions are deposited in the underlying substrate. A typical mask channel dimension is 25 nm wide, however, the damage straggle length from ion implantation is generally larger than the mask size. Figure 2.4 is a simulation of the stopping range of ions in matter (SRIM) [53]. This simulation shows the displacements in YBCO, showing the width of the disordered region compared to the mask.

Since the size of the junction is much greater than a typical tunneling length for electrons or holes and the coherence length, the conduction length for the masked ion beam irradiated junctions is much longer than the direct tunneling length of conventional SIS tunnel junctions. These junctions are "proximity junctions" when a metallic material is in proximity with a superconductor and if the electrons can

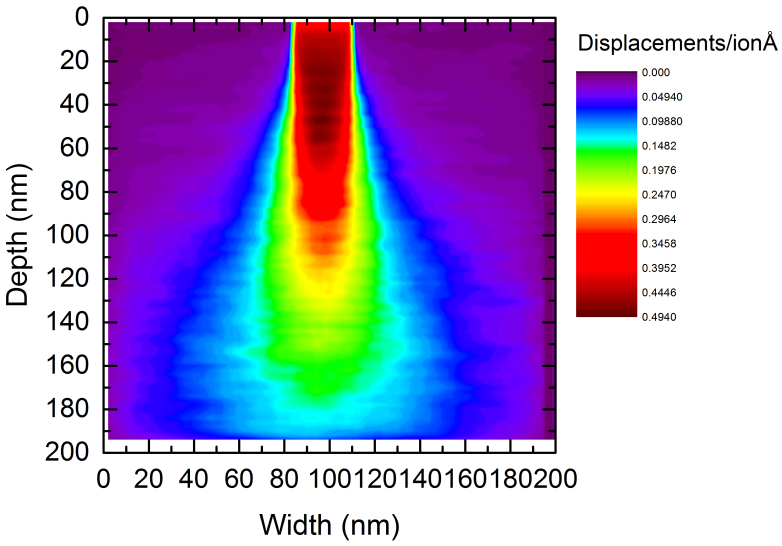

Figure 2.4: Displacement in a 200 nm YBCO film irradiated with 175 keV Ne^+ with mask channel 25 nm wide. The straggle length is 80 nm, greater than the channel width.

maintain time reversal symmetry while in the material, then superconductivity can proximity couple into the material. The proximity effect can only occur when there are allowed extended electron or hole states in the non-superconductor. In most cases, the material is a metal, but in masked junctions, the material is a lower T_C superconductor. The pair amplitude decays into the proximity coupled material. Since the proximity effect is a diffusive process, the length scale is much longer range than tunneling. Therefore, it is possible to have proximity coupled junctions with wider barriers ($\sim$ 100 nm) that is not insulating. This property explains the lower $I_C R_N$ product for masked junctions as R_N increases approximately linearly with defects but I_C decreases much faster than linear.

Proximity coupled junctions have weak barriers, such that an additional transport method for non-paired carriers, the quasi-particles, are activated. Andreev proposed that when an electron approaches a normal metal superconductor interface, a hole will reflect in the opposite direction from the interface, thus transferring 2e (the charge on a superconducting pair) though the interface into the superconductor [54]. This conduction method is called Andreev reflection, and is the source of

excess current (I_χ), observed in some junctions. This excess current has no magnetic field dependence and is undesired. For most SNS junctions at lower temperatures, I_χ is commonly and incorrectly included when reporting $I_C R_N$, and results in overestimated values for SNS junctions.

Blonder, Tinkham and Klapwijk (BTK) proposed a model for transport between a superconducting-normal metal interface that describes the transport mechanisms in terms of a barrier strength (Z) which changes from a metal-metal interface (weak Z) to a metal-insulator interface (strong Z) [55]. At a lower Z, Andreev reflection is the dominant transport for quasi-particles. When Z is close to unity, both tunneling and Andreev reflection exist as the conduction channel. In strong barriers ($Z > 1$), direct tunneling is the only mechanism possible. A follow-up work by Octavio *et al.* [56] attempted to adapt this model to a Josephson junction.

Based on previous studies by our group [41, 57, 46, 58] and the fact that the transport mechanism for SNS and SIS can be described by a microscopic single parameter theory, the metal-insulator transition should be observable in ion irradiated junctions. However, the junction barrier needs to be deeper and narrower (*i.e.* a transition from metal to insulator on an atomic scale).

Chapter 3

Focused Helium Beam Irradiated Josephson Junctions

3.1 Motivation

Previously, we have hypothesized that with narrower and higher Z barriers it is possible to observe the metal-insulator transition into the tunneling regime in ion irradiated junctions in YBCO. An SIS junction allowing in-plane tunneling and junction spectroscopy in the same material has not been previously accomplished.

In terms of junction fabrication technology, a stronger barrier should improve junction parameters, and a better-defined barrier will potentially increase the uniformity. However, with current masked ion irradiation technology described in the previous chapter, the feature size of the mask is limited to tens of nanometers at best. From previous simulations, even a mask of 24 nm has a disordered region that extends to about 100 nm. Therefore, a new approach needs to be implemented. Instead of using a mask and broad beam implant, we realized that a focused ion beam (FIB) may improve the feature size. Previously, researchers have adapted focused ion beams for nanopatterning and/or direct writing of the junction barrier [59, 60, 61, 62, 63]. The most common liquid metal source is gallium with a typical beam spot of $\sim$ 50 nm. Due to the spot size of the Ga beam, the atomic mass, and the beam energy, feature sizes from a liquid metal source are still limited to $\sim$ 100 nm. The junction parameters are similar to the masked ion irradiated junctions.

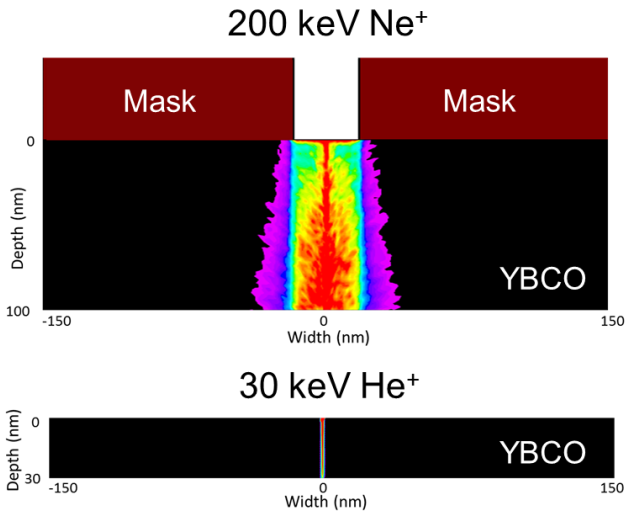

Figure 3.1: Simulated displacement in (a) 100 nm and (b) 25 nm YBCO with (a) 200 keV Ne^+ and (b) 30 keV He^+ using Silvaco Athena^{TM}to compare the junction size of masked implantation with focused ion beam.

In order to reduce the feature size, helium–a smaller inert atom–is an excellent candidate. ALIS^{TM}, now a part of Carl Zeiss Microscopy^{TM}, developed a gas field ion source (GFIS) for their helium ion microscope (HIM) in 2006 [64]. The spot size of the focused helium beam is 500 pm, smaller than conventional FIB by two orders of magnitude. Figure 3.1 shows the comparison of disorder profiles in a masked junction and a focused helium beam (FHB) junction. The disordered region generated by the helium beam is much smaller and more uniform than the masked junction. Furthermore, the barrier width created by the helium beam is similar to typical tunneling length for electrons or holes. From the simulation, we know it is possible to see a metal-tunneling transition in YBCO junctions. The following section will describe our experiments.

3.2 Fabrication

Devices were fabricated on 5 mm square sapphire substrates with *in-situ* 200 nm Au on 150 nm or 25 nm YBCO, where the YBCO is grown by reactive

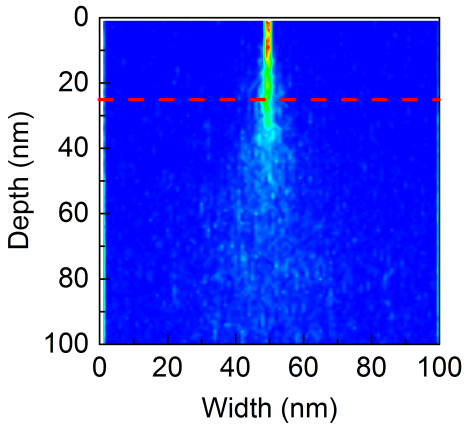

Figure 3.2: Simulation of 30 keV He^+ implanting into a 100 nm YBCO film. The red dash line indicates 25 nm deep in the YBCO. The displacement in the YBCO remains relatively uniform and the straggle is small for depths up to 25 nm.

co-evaporation and supplied to us from Ceraco^{TM}. Fabrication steps are described in the following. Firstly, standard photolithography and Ar^+ ion milling were used to define the electrodes as previously in chapter 2. Next, the thickness of YBCO needed to be determined for helium ions irradiation such that He^+ create damage without implanting helium in the YBCO film. Since the maximum He^+ energy from the microscope is 30 keV, the film thickness needs to be thin. The film thickness range was determined by SRIM simulation of 30 keV He^+ implanting a 100 nm thick YBCO film.

According to the SRIM simulation in figure 3.2, the helium ions penetrate approximately 25 nm of YBCO with very little lateral straggle and with uniform disorder density. Therefore, the thicker films need to be thinned to approximately 25 nm to meet the requirements. For the thicker films, photolithography was performed to define a window for a second ion milling process to thin the YBCO within the window where the junctions will be written. Resistance as a function of mill time was measured at room temperature to determine the thickness of the YBCO film after ion milling. Figure 3.3 shows a picture of the sample after two steps of processing. Each chip has four 4 μm bridges in a 4-point measurement configuration. The process only requires photolithography and chemical etch to remove the gold exposing the write field for the 25 nm-thick films. Figure 3.4 shows a picture of a thinner film sample

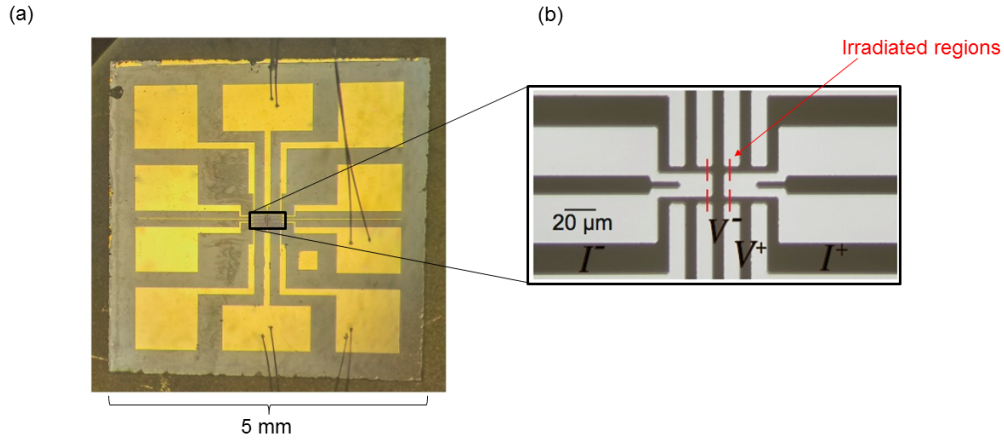

Figure 3.3: (a) A picture of the circuit on thicker YBCO films after two steps of processing. (b) A zoomed in view of the center write field showing four 4 μm bridges in a 4-point measurement configuration. The red lines indicate where the Josephson junctions were written with the focused helium beam.

that has twenty 4 μm bridges in a 4-point measurement configuration. Finally, the samples were irradiated with a helium ion beam as indicated in both figures 3.3(b) and 3.4(b) at different doses ranging from 50 ions/nm to 3000 ions/nm.

3.3 Measurement results

Measurements were done in a low noise cryogenic measurement system inside a shielded room. All I–Vs were taken where the junctions were current biased with a 1 Hz slow sweep from a function generator. Two separate preamplifiers were used to measure the voltage across the junction and the voltage across a known resistor in series with the junction in order to determine the current. The outputs of the preamps were then read by a DAC connected to a computer.

The first round of the experiment was done using the thinned down samples with four 4 μm bridge pattern (Fig. 3.3) in order to determine the thickness and to find the dose range for junctions, experimentally. I–V curves of 25 nm thick YBCO irradiated with 50 ions/nm (lowest) and 3000 ions/nm (highest) are shown in figure 3.5. The resistance of the lowest dose junction is less than 0.01 Ω while the resistance vs. temperature plot (RT) of the highest dose junction increases a few orders of magnitude. Junctions irradiated with 100 ions/nm and 300 ions/nm have an I–V

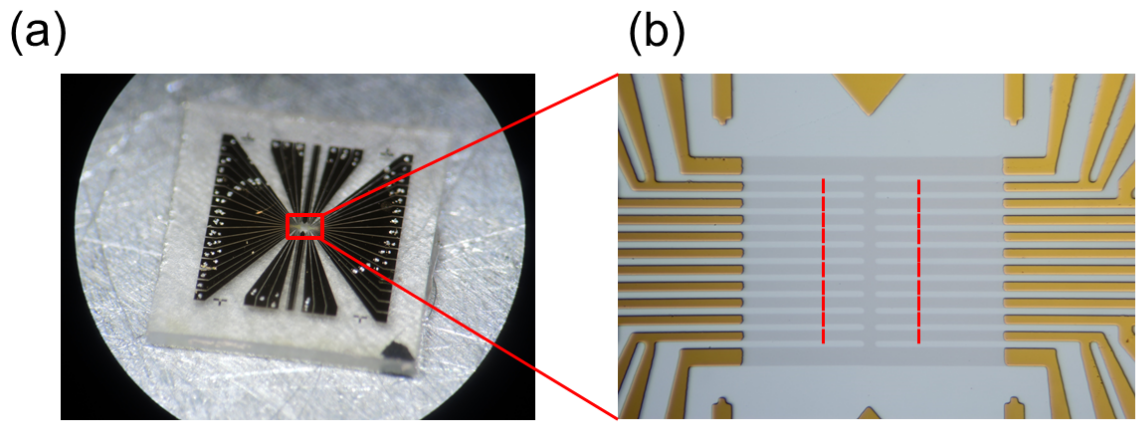

Figure 3.4: (a) A picture of a circuit on 25 nm-thick YBCO films after gold removal. (b) A zoomed-in view of the center write field showing twenty 4 μm bridges in a 4-point measurement configuration where the red lines indicate ion irradiation.

that corresponds to the RSJ model presented (Fig. 3.6(a), 3.6(d)). Figure 3.6(b) shows that the R_N of the 100 ions/nm junction decreases with lowering temperature from 0.9 Ω to 0.5 Ω. In addition, I_C rises as the junction temperature decreases. Figure 3.6(b) shows that R_N of the high junction increases with lower temperature from 8 Ω to 20 Ω for the junction irradiated with 300 ions/nm.

From the data presented, we have shown R_N for the 100 ions/nm junction resistance decreases with lower temperature, which suggests a metallic behavior. The resistance of the junction is $\sim$ 10 times higher resistance than masked junction, typically between 0.01 $\sim$ 0.1 Ω, as expected for a stronger Z barrier. Due to the increase in R_N, the $I_C R_N$ of SNS FHB junction is $\sim$ 10 times higher. In addition, the supercurrent increases similar to a power law [41] as the junction was cooled, a typical property of SNS junctions when the excess current I_χ from Andreev reflection is enhanced. On the other hand, R_N of the junction irradiated with 300 ions/nm increases with lowering temperature; this behavior reveals the first evidence that the junction barrier is an insulator while showing a Josephson current. Properties of the I_C provides more evidence that the barrier is an insulator. I_C approaches a maximum value at lower temperatures, similar to SIS junctions from conventional superconductors following the BCS theory. Furthermore, I_χ is not present in the I–V curves in figure 3.6(d). Therefore, we believe we have shown that both SNS and SIS

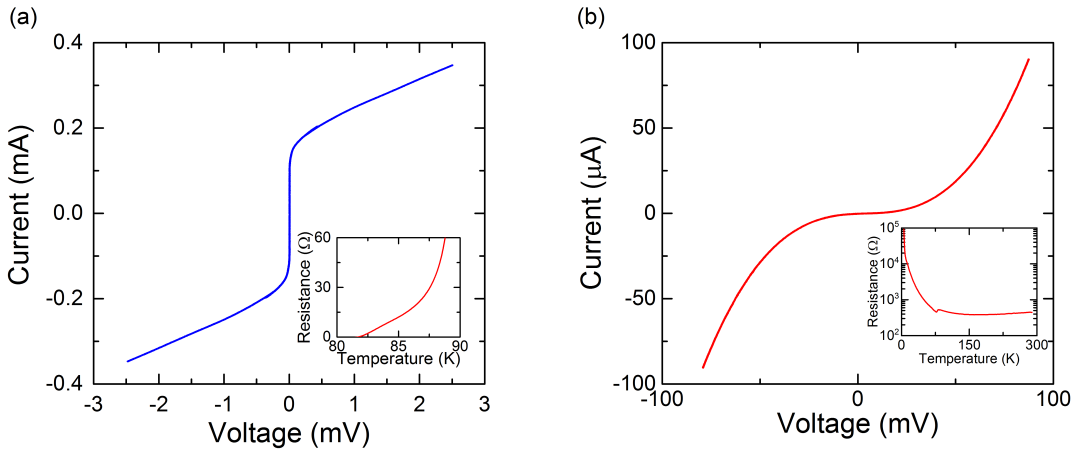

Figure 3.5: (a) I–V and (inset) resistance vs temperature plot of a line written with 50 ions/nm. (b) I–V and (inset) resistance vs temperature plot of a line written with 3000 ions/nm.

junctions can be made using an FHB.

To investigate the region near the metal-insulator transition, a second round of the experiment was done with a much finer dose range. Since a good thickness has been determined in the previous experiment, 25nm-thick film was the only thickness used in this experiment to simplify the fabrication process. Figure 3.4 show the sample design, twenty 4 μm bridges were patterned in the write field of the test samples. Junctions were irradiated in the range of 75 ions/nm to 425 ions/nm at 25 ions/nm increments. I–V curves were taken to extract the temperature dependence of R_{N} and I_{C}. I_{χ} was purposely included in I_{C} to illustrate the SNS junction. Figure 3.7(a) shows R_{N} as a function of temperature and the red line separates two different trends of temperature dependence. I_{C}s for junction doses higher than 325 ions/nm approach a constant value at lower temperatures, and I_{C}s for lower doses kept increases (Fig. 3.7(b)). A special case is the junction irradiated with 325 ions/nm, where R_{N} remains relatively constant over a very wide temperature range. Figure 3.8 shows the junction has no I_{χ} and $R_{\mathrm{N}} = 5.25\ \Omega$ with very small variations from 12.5 K to 43 K. The $I_{\mathrm{C}}R_{\mathrm{N}}$ value of this junction increases only with increasing I_{C} up to $\sim 350\ \mu$V.

Based on the data shown here, the electrical properties of barriers continuously changes from metallic to insulating by varying the irradiation dose. The metal-insulator transition in junction barriers corresponds well with the BTK model, where

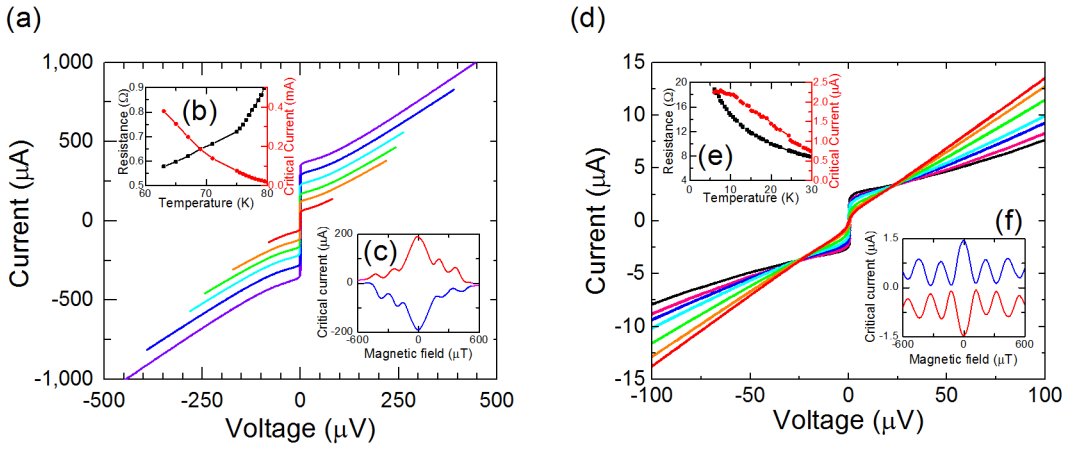

Figure 3.6: The temperature dependence of I–Vs of a junction written with (a) 100 ions/nm (d) 300 ions/nm measured from (a) 75 K to 63 K (b) 5 K to 25 K. (b)(e) The temperature dependence of I_{C} and R_{N}. (c)(f) The magnetic field dependence of I_{C} of the junction.

the barrier strength Z is controlled by the dose applied. The temperature range where the I_{C} is clearly visible in the I–V but before I_χ begins dominating the supercurrent is much larger than the masked junctions. This can be understood with a moving boundary model proposed by Katz *et al.* [41], which limits the temperature range in the case of masked junctions. However, for FHB junctions, the barrier is much narrower and well defined such that the junction width does not vary with temperature. Furthermore, for the higher dose SIS junction, there is no I_χ to limit the lower bound of the temperature range. A common conventional SIS tunnel junction usually has a hysteretic I–V curve, but the SIS junctions presented here do not have hysteretic I–Vs. This is because the area of the junction is much smaller than the conventional sandwich junctions such that β_C is small. The junction area in the current case is 25 nm by 4 μm. If we assume the barrier is 2 nm and we use the dielectric constant of sapphire, then we estimate the capacitance to be

$$C = \epsilon\epsilon_0 \frac{A}{d} = 10\epsilon_0 \frac{25\text{ nm} \times 4000\text{nm}}{2\text{nm}} = 4.4 \times 10^{-15}\text{F}. \tag{3.1}$$

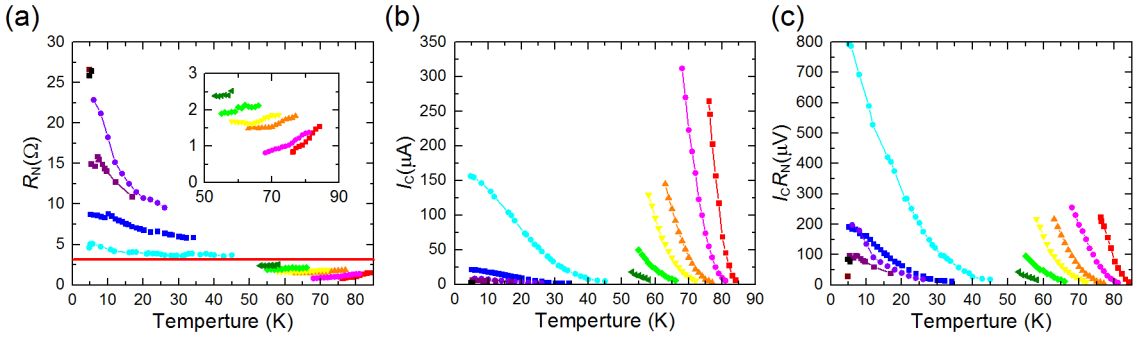

Figure 3.7: The temperature dependence of junctions written with dose from 75 ions/nm (red) to 425 ions/nm (black) at an increment of 25 ions/nm. (a) The red line separates resistance increasing with lower temperature (above) and decreasing with lower temperature (below). (b) I_C approaches a constant at higher doses, and diverges at lower doses as temperature decreases. (c) Junction I_CR_N parameter space across a range of 80 K in temperature.

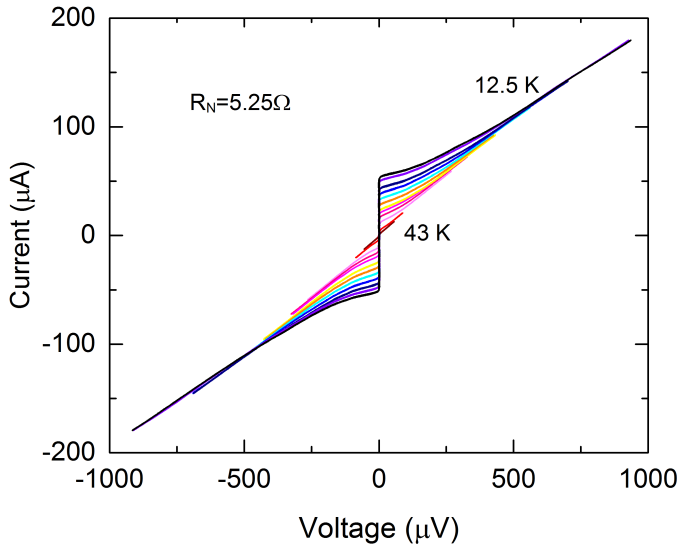

Figure 3.8: I–V of a junction written with 325 ions/nm. The junction exhibits a constant resistance of 5.25 Ω over a 30 K range.

Therefore, following Eq. (1.26), the junction β_C is

$$\beta_C = \frac{2e}{\hbar}(3\ \mu\text{A} \times 19\ \Omega)(19\ \Omega \times 4.4 \times 10^{-15}\text{F}) \approx 0.014. \tag{3.2}$$

Hence we believe the junction is in a non-hysteretic, overdamped regime. In figure 3.7(c), the FHB junctions have large $I_C R_N$ space over a large temperature range without changing any other parameters: for example, the bridge width and film thickness. Lastly, in the special "crossover" case shown in figure 3.8, it is near the middle of the metal-insulator transition. The resistance of the junction remains constant over 30 K. For the same $I_C R_N$ value, higher dose gives more resistive junctions.

3.4 Dynamic conductance in planar YBCO junctions

There have been several studies of the energy gap of HTS with tunneling spectroscopy [65, 66, 67, 68]. However, those experiments were usually performed with c-axis tunneling with an STM or with a conventional superconductor-YBCO tunnel junction. As described in the previous section, the higher dose FHB junctions have resistances high enough so that it is possible to bias the junction to previously reported gap voltages and conduct spectroscopy in the ab-plane with a YBCO-YBCO junction. The dynamic conductance (σ) of the junctions is the derivative of the I–V ($\frac{dI}{dV}$) which is the measures the two convoluted density of states. To measure the derivative experimentally, a 2.2 kHz 0.1% $\sim$ 1% modulation was added on the 0.1 Hz slow sweep bias current for the I–V measurement. The modulation of the current is the dI and the oscillation voltage is the dV in the derivative of $\sigma = \frac{dI}{dV}$. There are two frequency components in this experiment to measure the DC current and voltage. The low-pass filter of the two preamplifiers was set to 100 Hz to filter out the modulation. A second set of preamplifiers was used to measure the higher frequency signal dI and dV with the high pass filters set to 300 Hz. The outputs of the two DC preamplifiers were still read by the DAC, as in the previous I–V measurements, but the two AC preamplifiers were connected to two synchronized lock-in amplifiers. A lock-in amplifier converts an AC signal amplitude to a DC voltage. The ratio of the

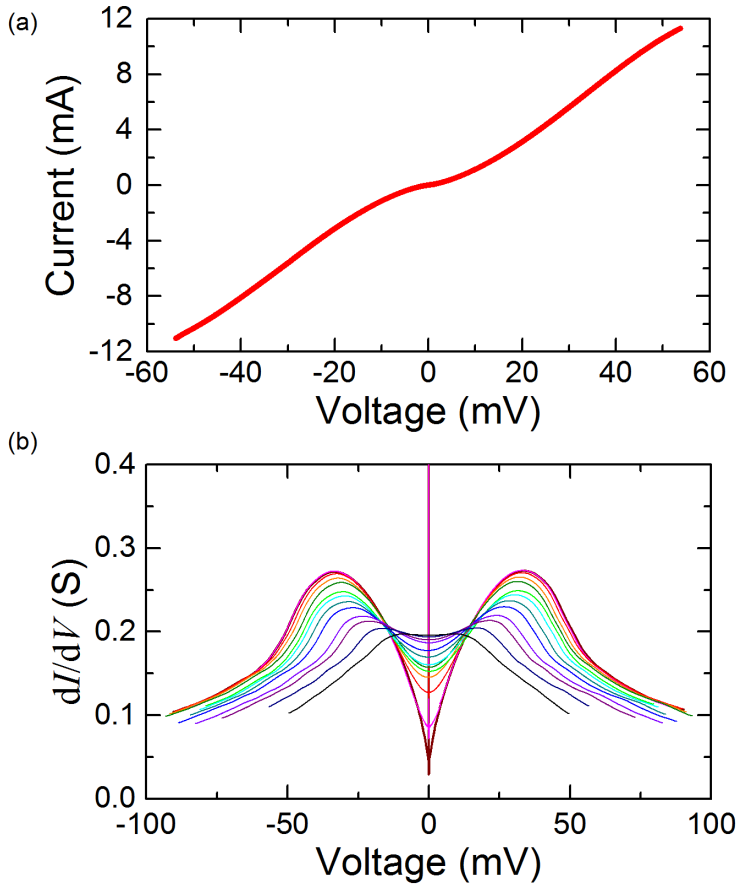

Figure 3.9: (a) I–V the junction in figure 3.6(d) biased to 60 mV. (b) The dark red line is the derivative of (a) measured with a lock-in amplifier at 5 K. Different colored lines represents the derivatives of temperature between 5 K to 75 K.

dI and dV amplitudes from the lock-in amplifiers were then simultaneously recorded with the current and the voltage by the DAC. Figure 3.9(a) shows the I–V of the SIS junction in figure 3.6(d) biased up to 60 mV at 5 K. Dynamic conductances as a function of junction voltage at temperatures below T_C, ranging from 5 K to 75 K, were plotted in figure 3.9(b). The lowest two-temperature dynamic resistance and I–V was taken at multiple bias ranges, and then combined in one plot to capture the critical current. For these gapless superconductors, it is common to define the peak of the dynamic conductance to be the energy gap-like value. Therefore, we fitted the peak value extracted from figure 3.9(b) with the equation for the temperature

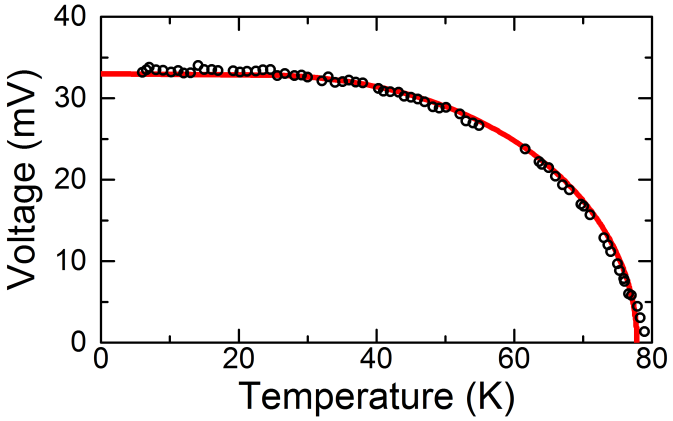

Figure 3.10: Temperature dependence of the peak dynamic conductance extracted from figure 3.9 (black circle). The red line is the data fitted with Eq. (3.3).

dependence of the gap from BCS theory in figure 3.10, to obtain

$$\frac{1}{N(0)V} = \int_0^{\hbar\omega_C} \frac{\tanh \frac{1}{2}\beta(\xi^2+\Delta^2)^{1/2}}{(\xi^2+\Delta^2)^{1/2}} d\xi, \tag{3.3}$$

where $\beta = \frac{1}{k_B T}$, $N(0)$ is the density of state at the Fermi level, and ω_C is the cutoff frequency. While we understand that defining this quantity as the "energy gap" only applies to an isotropic conventional (s-symmetry) superconductor, we find it quite interesting that this general form of an order parameter fits so well.

In this section, we presented data showing the spectroscopy of the same SIS junction shown in figure 3.6(d). Since the conductance is infinite ($\sigma = \frac{dI}{dV} = \infty$) below I_C, at $V = 0$ a large peak representing the supercurrent is present at zero voltage in figure 3.9(b). At 5 K, the finite voltage peak occurs at 33 mV as both electrodes are YBCO the and voltage represents 2Δ of YBCO. In BCS theory, the value $\frac{2\Delta}{k_B T_C} \simeq 3.52$ is similar for weak coupled superconductors. However, the value varies wildly for HTS materials. In our case, $\frac{2\Delta}{k_B T_C} = 4.8$ where T_C is 80 K. Our measured value is within the range reported in the literature $2\Delta = 15 \sim 35$ mV [66, 65]. The difference in the gap-like voltage is believed to be due to the variation of the YBCO film quality and the nature of the s and d-wave symmetry order parameter. Although YBCO is a gapless superconductor, the peak dynamic conductance follows the temperature dependence of the BCS theory. Other reports have shown similar

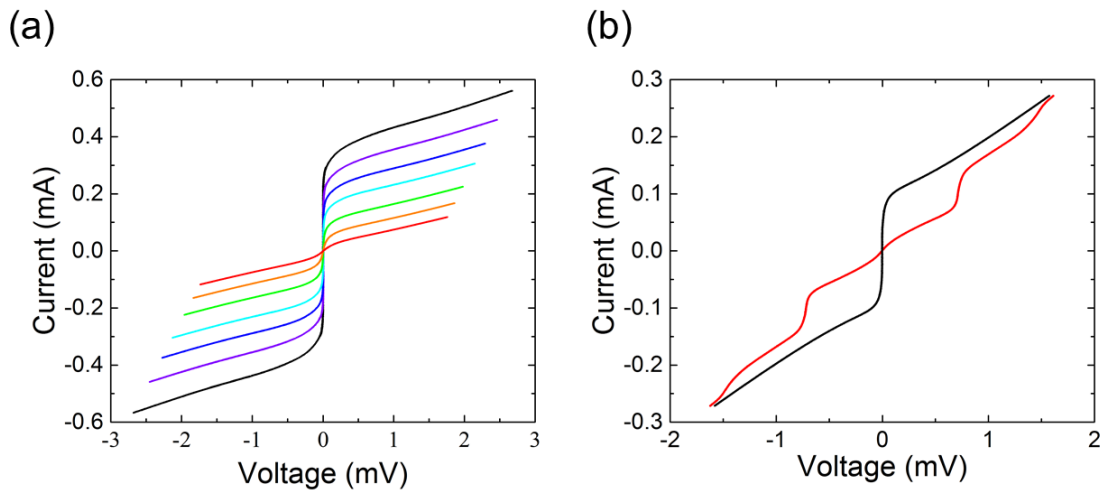

Figure 3.11: (a) I–V curves of junction array written with 100 ions/nm taken at temperatures between 62 k and 78 K indicated by the colors. The resistances dropped from 17 Ω to 13 Ω as temperature decreased. (b)The black curve shows the I–V without RF signal irradiation, and the red shows I–V irradiated with 17.589 GHz RF signal. The I–Vs were measured at 77 K.

temperature dependence of the gap-like peak. This result suggests that the pairing mechanisms for HTS has some similarities with conventional superconductors and requires further investigation.

3.5 Uniformity

In addition to the individual characteristics of the junctions, in order to build a better understanding of the physics of HTS, we also studied the uniformity of the arrays for application purposes. The "bottle neck" in HTS electronics has been the lack of fabrication technology for reproducible uniform Josephson junctions that is easily scalable. Here we look at the reproducebility of FHB Josephson junctions with 1D arrays. Twenty junctions were written in a bridge for the sample shown in figure 3.3. I–V curves of an array written with 100 ions/nm for each line, taken at different temperatures, are shown in figure 3.11(a). Figure 3.11(b) shows the array irradiated with a 17.589 GHz external RF signal, and the resultant Shapiro step occurs at 0.725 mV. A second junction array with same number of junctions was written with 300 ions/nm, as shown in figure 3.12(a), where the resistance of the junction is 450 Ω

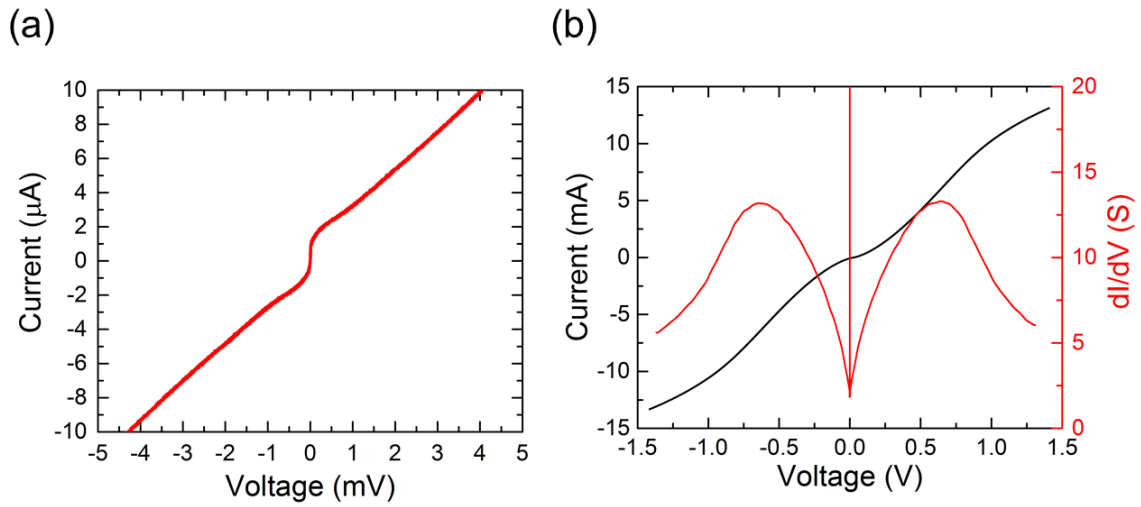

Figure 3.12: (a) I–V of 20 junction array irradiated with 300 ions/nm measured at 4 K. The resistance of the array is 450 Ω. (b) The black curve is the I–V at 4 K biased to 1.4 V. The red curve is the dynamic resistance of the I–V curve, and the dynamic conductance peak occurs at 0.66 V.

at 4 K. The dynamic resistance of the array was measured up to 1.4 V and the peak occurs at 0.66 V.

We have shown that a SNS junction array irradiated with RF signal exhibits large Shapiro steps. From Eq. (1.11), the first step should occur at $20 \times \frac{h17.589\ \text{GHz}}{2e} = 0.727$ mV, which is very close to the experimental value 0.725 mV. In order to show a vertical step, the resistance of each junction in the array must be the same; otherwise, junctions will reach the step voltage at different bias currents. Also in the voltage state of I–V curves, this I–V characteristics has the upward curvature from the RSJ model. Compare with the masked junction array by Cybart *et al.* [46], which has a 16% spread in I_C and the I–V is less RSJ like. The I_C spread in the SNS junction array should be less than 16%. As for the SIS junction array, the peak conductance appears at 0.66 V, 20 times the single junction peak voltage. Both the SNS and the SIS junction array suggest the variation between the junctions is small.

3.6 Conclusion

In this chapter, we tested our hypothesis that if the junction barrier is narrow enough and disorder density results in a high enough Z, we can observe the metal-insulator transition in the junction. With a focused helium beam that has a spot size of 0.5 nm, we made junction barriers exhibit both metallic and insulating behavior. By changing the dose for each junction, we also showed the electrical properties of junction barriers transition continuously from a metal to an insulator. We observe a special case where the junction barrier is near the metal-insulator transition, and has a constant resistance for a very large temperature range. Overall, the junction $I_{\mathrm{C}}R_{\mathrm{N}}$ is much higher than the masked junctions because the barrier is stronger and very well-defined. The amplitude of the order parameter does not decay as in a SNS junction of chapter 2. The barrier size can be inferred from our measurements of the dynamic conductance, and the peak value is within the value reported in the literature. Also, the peak conductance has the same temperature dependence as the energy gap of BCS superconductors. The unique part of this experiment is that the dynamic conductance was measured in the ab-plane of a YBCO-YBCO junction and there is no different-material interface. Although variable range hopping in the damaged barrier has not been excluded, the junction barrier size is limited to its tunneling length and a conduction path via variable range hopping would not show a Josephson current. In addition to the higher quality junctions, the uniformity is also better, and the fabrication step is greatly simplified. It is possible to perform wafer scale processing with this technology to make highly uniform junctions at affordable time and costs.

3.7 Acknowledgement

Chapter 3, in part, has been submitted for publication of the material as it may appear in *Nature Nanotechnology*, 2015, S. A. Cybart, E. Y. Cho, T. J. Wong, B. H. Wehlin, M. K. Ma, C. Huynh, and R. C. Dynes, Nature Publishing Group, 2015. The dissertation author was the primary investigator and author of this paper.

Chapter 4

Nanowires

4.1 Motivation and fabrication techniques

Most of the previous HTS-HTS junctions are non-hysteretic or overdamped junctions due to the nature of the junction barrier. Also, in most applications a non-hysteretic junction is more stable and better controlled. However, with the new SIS FHB junctions it should be possible to reproduce all the different conditions in LTS junctions. In the previous chapter, we estimated β_C to be much less than 1. If the junction dimension is modified to increase the resistance or capacitance, it should be possible to observe underdamped junction characteristics. In addition, the parameter space showed in figure 3.7(c) is limited to a junction width of 4 μm. Reducing the junction width is one possibility to expand the parameter space while remaining in the short junction limit.

Currently the smallest feature size in HTS superconducting electronics is limited to micron-sized features because there is no good chemical etch or RIE currently available. HTS materials are extremely sensitive to processing, and the superconducting properties can be easily altered. Chemical etching can only be used on large features above tens of microns. The primary etching method is dry etching with isotropic Ar^+ milling. However, overheating of the material by ion milling causes deoxygenation and in most cases, the process transforms the superconductor into an insulator. Therefore, dry etch is required for smaller feature sizes but limited to a few microns. Recently there have been advancements by using protective layers

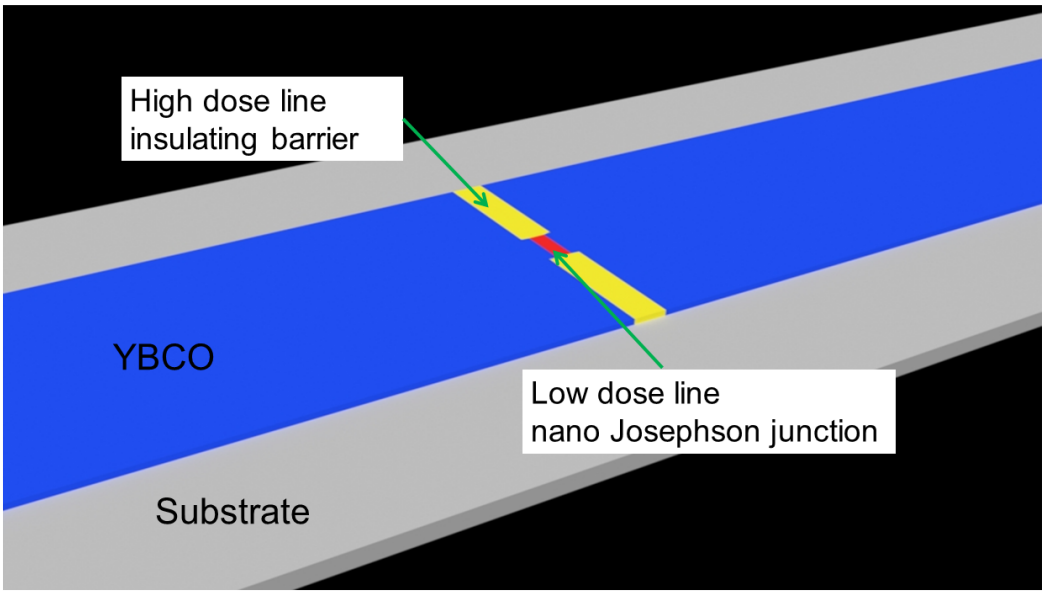

Figure 4.1: A schematic of a nanojunction on 25 nm-thick YBCO. The red line indicates the junction barrier written with lower dose. The yellow line indicates the insulating region to define the junction width written at a higher dose.

in fabricating nano wires [69]. Since we have demonstrated the nano-scale metal-insulator transitions in YBCO, applying the same principle it is possible to define the current path by an insulator created by helium beam irradiation. Because the dose required to disorder without removing YBCO is much less than milling, deoxygenation is less likely to happen. The nano pattern can be done at the same time as creating junctions, which greatly simplifies the fabrication process. Figure 4.1 shows a conceptual schematic of a nano junction. The micron size bridge is still prepared by photolithography, but the entire chip in theory can be patterned with an ion beam. Two insulating lines were written with 1000 ions/nm after the junction line was written to avoid charging. The gap between two insulating lines is the junction width. To determine the actual junction width, we use two different metrics. One is the scaling of $I_C R_N$ and the other is the magnetic field dependence of the critical current from Eq. (1.22) (the Fraunhofer pattern). The critical currents were measured with a technique called sample-and-hold. When the I–V exceeds the threshold voltage, the current value is recorded to be the critical current at that magnetic field. The I–V was swept at 10 Hz while the magnetic field was swept at 0.01 Hz. Therefore,

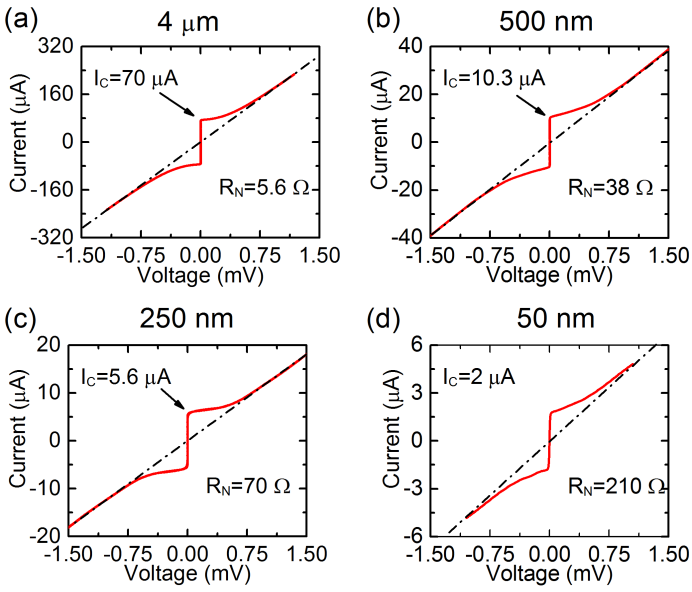

Figure 4.2: I–V curves of junction width (a) 4 μm, (b) 500 nm, (c) 250 nm, and (d) 50 nm. Each junction has $I_C R_N = 400$ μV and was irradiated with 300 ions/nm.

the magnetic field is considered a constant field for a single sweep of I–V. In this chapter we will explore the limits of this nanopatterning feature and the RSCJ model in YBCO junctions.

4.2 Measurement results

Samples with junction width from 4 μm to 25 nm were prepared measured in a vacuum cryostat in a helium storage dewar. Figure 4.2 shows I–V curves of 4 μm, 500 nm, 250 nm, and 50 nm wide junctions, where the 4 μm wide is the control with no nanopatterning. All the junctions have the same $I_C R_N$ value of approximately 400 μV. The critical current of the junctions are 70 μA, 10.3 μA, 5.6 μA, and 2 μA, respectively. As the junction width narrows, I_C decreases proportionally with the width of the junctions ($I_C \propto w$). Similarly, the normal state resistances of these junctions are 5.6 Ω, 38 Ω, 70 Ω, and 210 Ω, respectively. The R_N scales inversely proportional to the width of the junction ($R_N \propto \frac{1}{w}$), as expected. A second set of junctions with widths of 4 μm, 3 μm, 2 μm, and 1 μm were prepared to measure the magnetic field dependence of the critical current. The first minimum for each

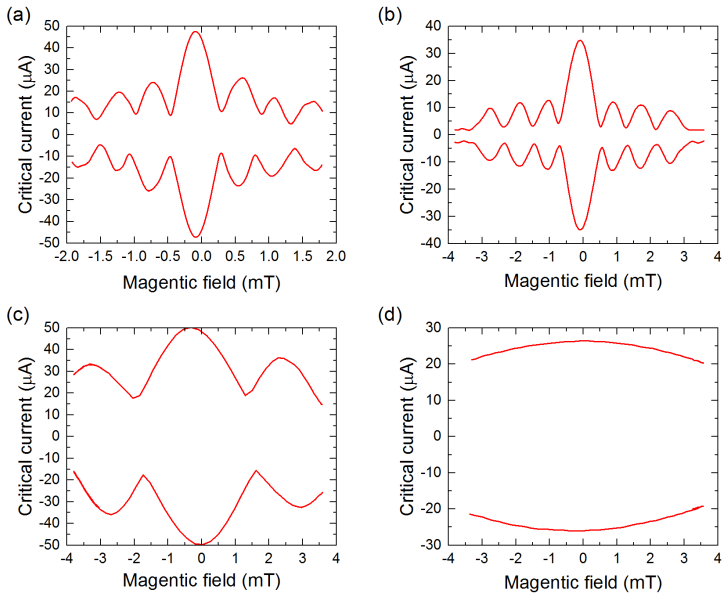

Figure 4.3: $I_C(B)$ of (a) 4 μm, (b) 3 μm, (c) 2 μm, and (d) 1 μm wide junction. The oscillation period increases as junction width decreases.

junction occurs at 0.3 mT, 0.5 mT, 1.6 mT, and $>$ 3.7 mT, respectively. Due to the maximum magnetic field range, the period of the 1 μm wide junction is beyond the measurable range of our *in-situ* magnet. However, the magnetic field period of the critical current modulation in figure 4.3 increases with smaller junction size. Using this FIB technique, we were able to make a 25 nm wide junction. In figure 4.4, we show an I–V of a junction narrowed down to 25 nm at 4 K. The resistance of this 25 nm-wide junctions is about 600 Ω, higher than the value from the 50 nm-wide junction. Unfortunately, the I_C is only approximately 25 nA but we can clearly observe the nonlinearity of the I–V characteristic of a noise rounded critical current.

The $I_C R_N$ of the nanojunctions in figure 4.2 are approximately the same. This indicates that the quality of YBCO remains high even after the nanopatterning. Because the dose required to disorder YBCO is much less than to completely mill it away, there is no deoxygenation due to heating during helium ion irradiation. Also, the scaling of R_N suggests the current flows only through the nanoconstriction between the two insulating lines. The measurement of $I_C(B)$ in figure 4.3 also supports the modified junction widths. However, the junctions are surrounded with the same

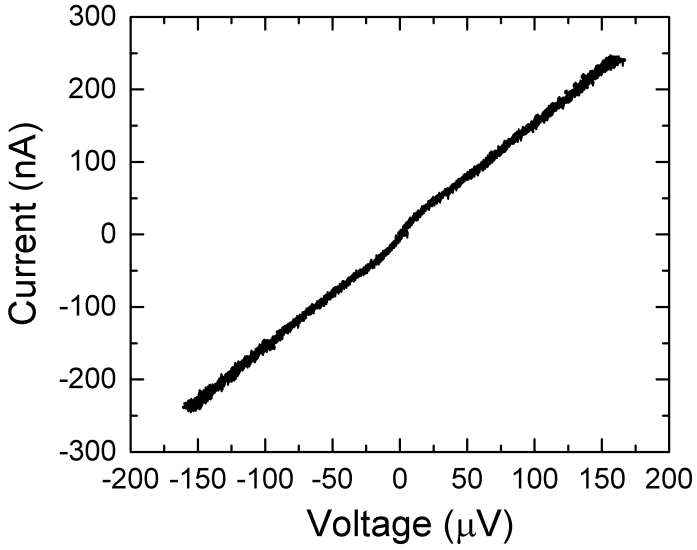

Figure 4.4: I–V of a 25 nm wide junction at 4 K with $I_{\mathrm{C}} \approx 25$ nA.

superconducting material from the bridge. Therefore, the geometry of the bridge plays a partial role in the $I_{\mathrm{C}}(B)$ through flux focusing [70].

To test the RSCJ model, β_C needs to be on the order of unity to see the properties of underdamped junction (resulting in hysteresis). Since β_C is proportional to R_{N}^2, it is simpler to change R_{N} and keep capacitance constant. R_{N} can be increased with higher irradiation dose and/or narrower junction width. Both can be done with the helium ion beam. Samples with junction width of 4 μm, 100 nm, 75 nm, and 50 nm were irradiated with dose 400 ions/nm, and R_{N} are 20 Ω, 208 Ω, 172 Ω, and 217 Ω, respectively. Figure 4.5 illustrates the I–V of junctions with different widths. The insets of each plot zoom in near I_{C}. All of the nanojunctions show a hysteretic characteristic in the I–V curves. Taking the 50 nm wide junction as an example, and using the same assumptions in Eq. (3.1) and (3.2) to estimate β_C of the junction. The capacitance is the same because the total bridge width is the same, but the resistance is much higher. Thus, β_C is now

$$\beta_C = \frac{2e}{\hbar}(6\ \mu\mathrm{A} \times 217\ \Omega)(217\ \Omega \times 4.4 \times 10^{-15}\mathrm{F}) \approx 3.8. \tag{4.1}$$

Similarly, β_C for the 100 nm and 75 nm junctions are between 4 and 5. The resistance of the nanojunctions are $10 \sim 20$ times larger than the 4 μm wide junction. Therefore,

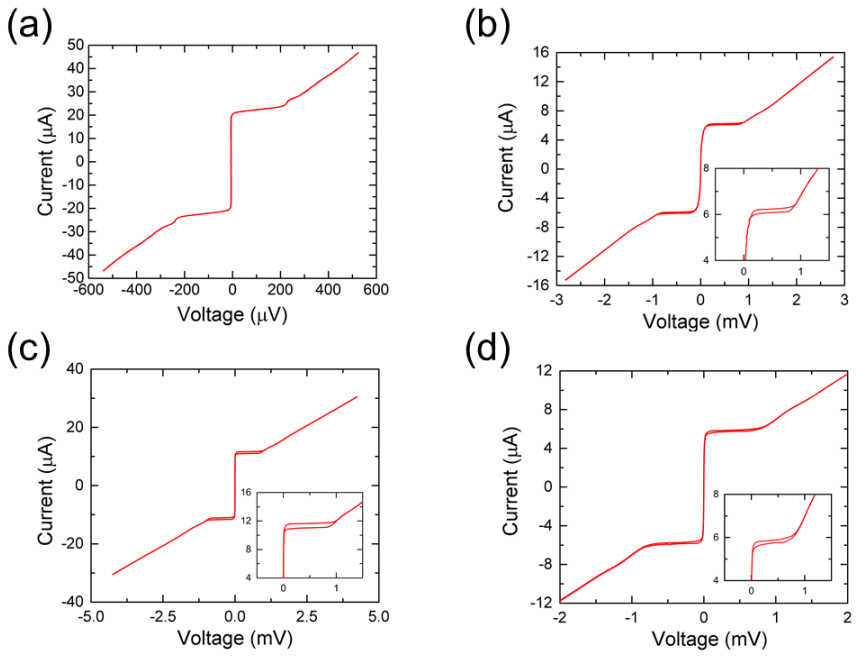

Figure 4.5: I–V curves of junctions irradiated with 400 ions/nm at 4 K. (a) A 4 μm wide junction as a control. (b), (c), and (d) are 100 nm, 75 nm, and 50 nm wide junction, respectively. In the inset of each nanojunction, the curve near I_C is displayed to show the hysteretic behavior.

the β_C of the nano junctions are a few hundred times larger than the value in Eq. (3.2) (above $\beta_C = 1$). Figure 4.6 shows the normalized I–V of the 50 nm wide junction and solutions of Eq. (1.25) with β_C from 0.2 to 3.3. The measured I–V falls within the range of $\beta_C = 1.7$ and $\beta_C = 3.3$, which is similar to the estimated value of β_C.

4.3 Conclusion

We have demonstrated that nanopatterning with a focused helium ion beam can create junctions as small as 25 nm wide. This technique shows no sign of material degradation from processing. It has not only expanded the $I_C R_N$ parameter space even further, but also the control over the ratio between I_C and R_N. A typical downside of superconducting electronics is impedance mismatch with standard conventional electronics. We have demonstrated junction R_N up to 600 Ω, potentially having superconducting electronics without mismatch to semiconductors. Previous HTS junction technologies have low resistance and small cross section area junctions,

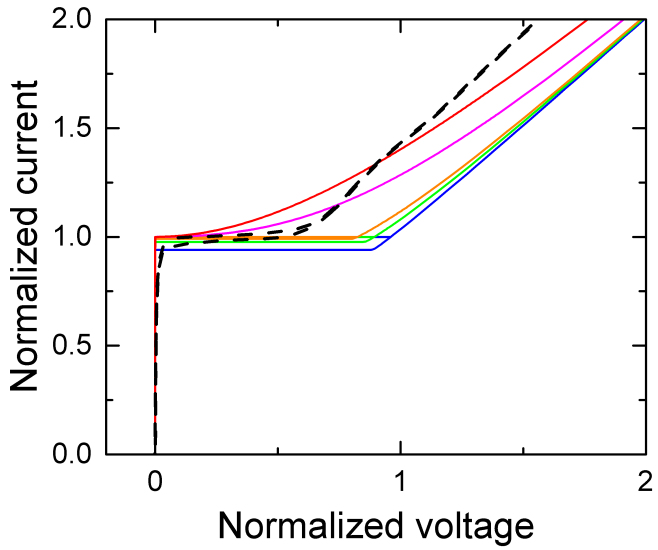

Figure 4.6: Simulated RSCJ I–V with $\beta_C = 0.2$ (red), 0.7 (magenta), 1.7 (orange), 2.2 (green), and 3.3 (blue). The dashed line is the measured I–V of the 50 nm junction in figure 4.5(d) where I and V are normalized by I_{C} and $I_{\mathrm{C}}R_{\mathrm{N}}$, respectively.

resulting a very small β_C. Through the control of R_{N}, we also observed underdamped junctions in YBCO. In principle, it is possible to have nanojunctions on a wider bridge to enhance the hysteretic behavior of the junction I–V (by increasing capacitance). In summery, we have developed a nano patterning technique that is faster and creates less damage to the material properties with a feature size less than 25 nm. With this technique, we have control over I_{C}, R_{N}, and β_C of the junction.

4.4 Acknowledgement

Chapter 4, in part, has been submitted for publication of the material as it may appear in *Microscopy and Microanalysis*, 2015, E. Y. Cho, Meng K. Ma, Chuong Huynh, R. C. Dynes, and Shane A. Cybart., Microscopy and Microanalysis, 2015. The dissertation author was the primary investigator and author of this paper.

Chapter 5

Order Parameter Symmetry of YBCO

5.1 Motivation and fabrication methods

The nature of a d-wave symmetry order parameter of YBCO has been of interest in the field of superconductivity since the discovery of high-T_C cuprates [71, 72, 73, 74]. Previously, there have been numerous studies using LTS-HTS junctions [75, 76] or scanning tunneling microscopy (STM) [66, 77] to probe the spatial dependence of the energy gap and the order parameter symmetry. However, these methods introduce additional variables and complications to the system. For example, when using a scanning tunneling microscope, the tip approaches a YBCO films or crystal in the c-axis, while YBCO is believed to have $d_{x^2-y^2}$ symmetry and the conduction path is in the ab-plane. Another example is using a YBCO-conventional superconductor junction where there is different material interface involved. In chapter 3, we have demonstrated in-plane tunneling spectroscopy with YBCO-YBCO junctions. It is now possible to test the order parameter directly in the conduction plane without scattering interfaces or with different materials involved. Another indicator for the order parameter is the $I_C R_N$ product; for conventional superconductors, the $I_C R_N$ product represents the gap energy. By combining the nanojunction technology described in chapter 4, the device can be reduced to a nanoscale size and so the junction cab be contained in a single grain boundary. In addition, the size of

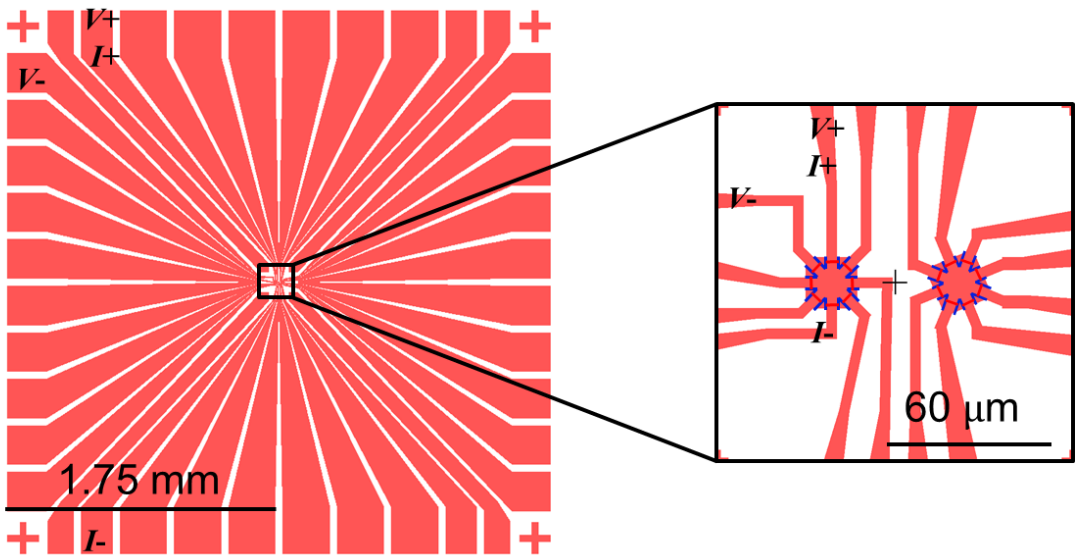

Figure 5.1: A layout schematics of the sample. In the center there are two squares with 8 bridges orientated in different directions. The blue lines indicates the insulating lines to define the junction width and current paths, while the red lines are the junctions.

the junctions allow us to increase resolution. In this chapter, we will probe the order parameter symmetry in the ab-plane with different size junctions, in hope to plot the angular dependence of $I_C R_N$ of YBCO.

Figure 5.1 shows the layout of the devices that were fabricated for measuring junctions at different orientations. The devices have two squares with eight 4 micron bridges that are rotated 45° from one another, and the two squares are at 22.5° from each other. To further reduce the size of the experimental region, high dose damage lines were written in the two squares to define the junction width and current paths. This design allows a 4-point measurement setup if and only if all the electrodes are superconducting, *i.e.* no lead resistance from the electrodes. In order to perform a 4-point measurement, a voltage probe and a current lead share the electrode that is connected to the junction being measured, while the other voltage probe and current lead can be connected on any of the other bridges, as shown in figure 5.1. In this experiment, junction widths of 4 μm, 3 μm, 2 μm, 1 μm, 500 nm, and 250 nm were patterned, and the junctions were created with an irradiation dose of 300 ions/nm.

5.2 Measurement results

The samples were measured in a cryogenic measurement system at 4 K. *I*–*V* curves of each junction were measured to extract the junction parameters I_C, conductance ($G = \frac{1}{R_N}$) which is the slope of the linear part of the *I*–*V*, and $I_C R_N$. Figure 5.2 shows, in a polar plot, the critical I_C as a function of junction orientation ($I_C(\theta)$) for junction widths of 4 μm, 3 μm, 2 μm, 1 μm, 500 nm, and 250 nm. Similarly, in figure 5.3, the conductance of the junctions is illustrated at different angles ($G(\theta)$). Starting from junction width less than 1 μm, we observed the appearance of nodes with very small conductance and I_C. Lastly, figure 5.4 shows $I_C R_N$ as a function of angle ($I_C R_N(\theta)$). The *I*–*V* curves of three 250 nm junction at different angles are shown in figure 5.5 to illustrate the variation. The curve at 22.5° (Fig.5.5(a)) shows no supercurrent at 4 K with a typical insulating *I*–*V* characteristics. While at 135°, $I_C \sim 4$ μA and $R_N \sim 50$ Ω with *I*–*V* typical characteristics of an RSJ model junction. Furthermore, the junction at 180° in figure 5.5(c) has very high $I_C R_N$ with a value of approximately 1 mV. This is a much higher value than most HTS junctions with exception of few bicrystal junctions reported in the literature.

5.3 Discussion and analysis

From the data presented, smaller junction structures exhibit larger junction parameter anisotropy for different orientations. All of the junctions with widths less than 1 μm have obvious nodes in the $I_C(\theta)$, suggesting that there are few or no states allowed for a particular $\boldsymbol{k}$ or no Josephson current in those directions. The most striking result comes from the feature of $G(\theta)$ of the 250 nm-wide junction. $G(\theta)$ hints the $d_{x^2-y^2}$ symmetry with three lobes and clear nodes. The $I_C R_N$ product of 1 μm and 250 nm wide junctions also show distinctive nodes and lobes that have the resemblance of d-wave symmetry. Even though, for gap-less HTS materials, the $I_C R_N$ product is more likely to be the collective result of the density of states and peak gap energy, it should have the order parameter symmetry. While the smaller junctions show features in $I_C(\theta)$, $G(\theta)$, and $I_C R_N(\theta)$, the junction parameters of the larger junctions are more relatively uniform in all orientations. In figure 5.6, we show the

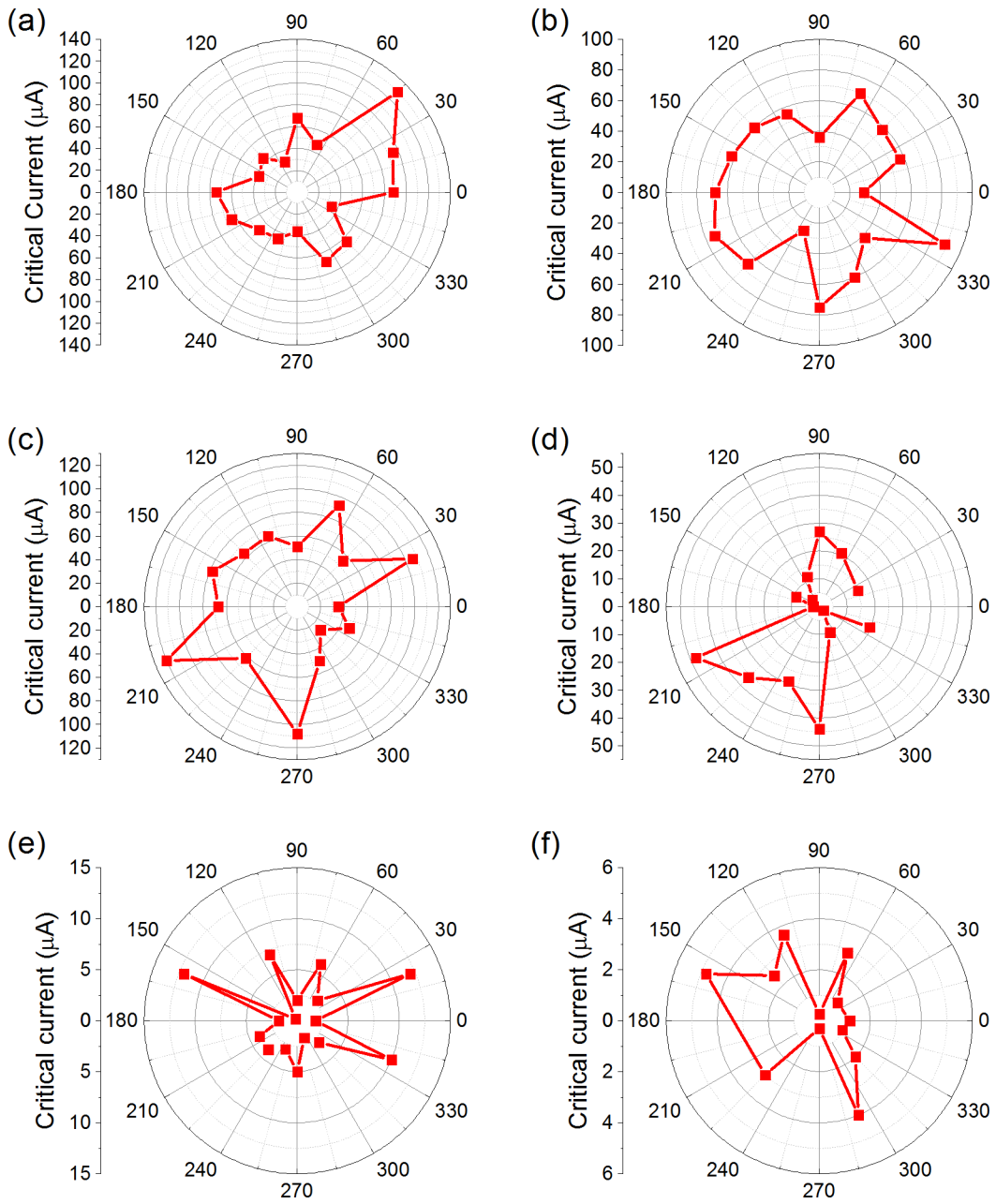

Figure 5.2: Critical currents of (a) 4 μm, (b) 3 μm, (c) 2 μm, (d) 1 μm, (e) 500 nm, and (f) 250 nm wide junction in different directions.

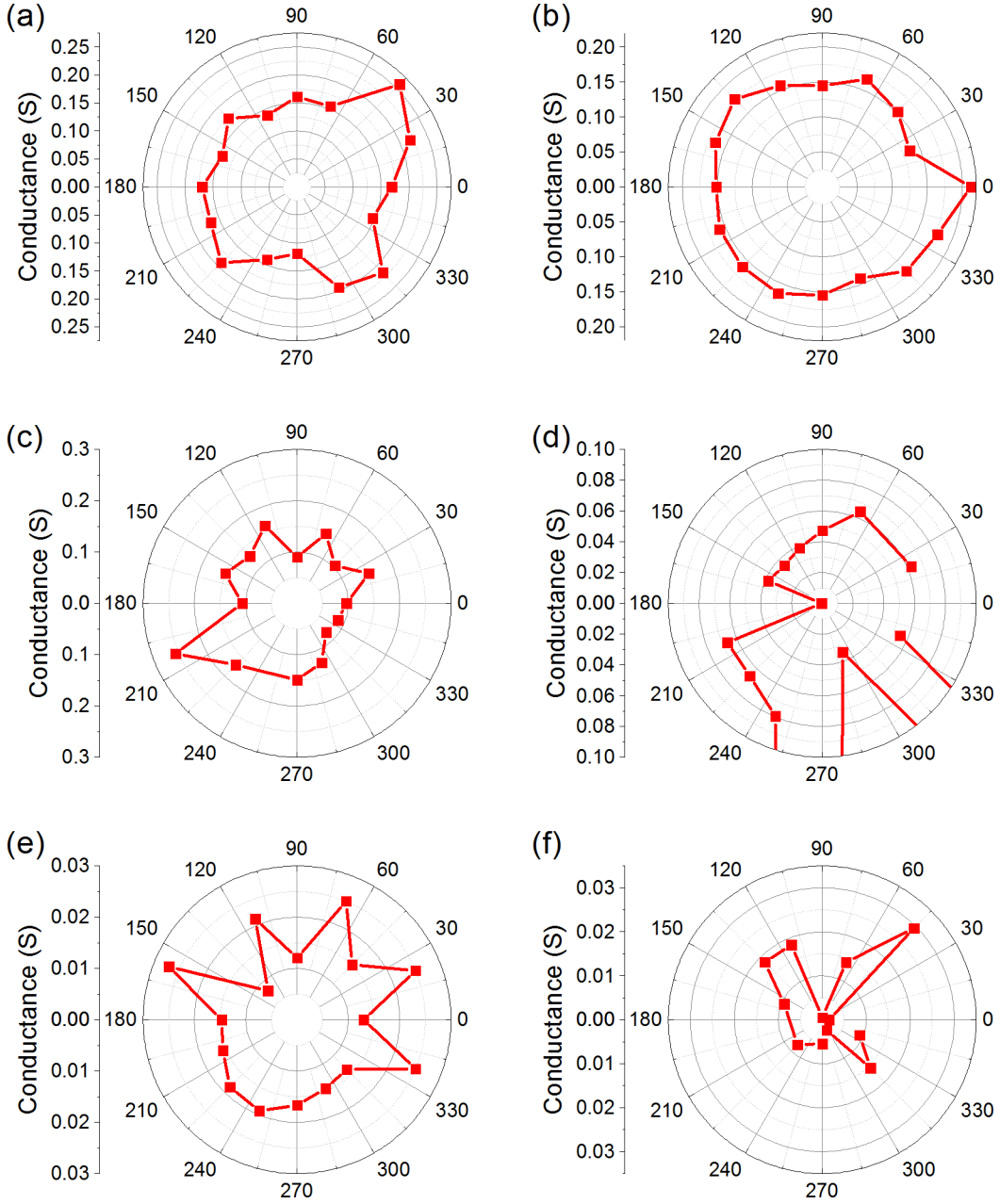

Figure 5.3: Conductance of (a) 4 μm, (b) 3 μm, (c) 2 μm, (d) 1 μm, (e) 500 nm, and (f) 250 nm wide junction in different directions.

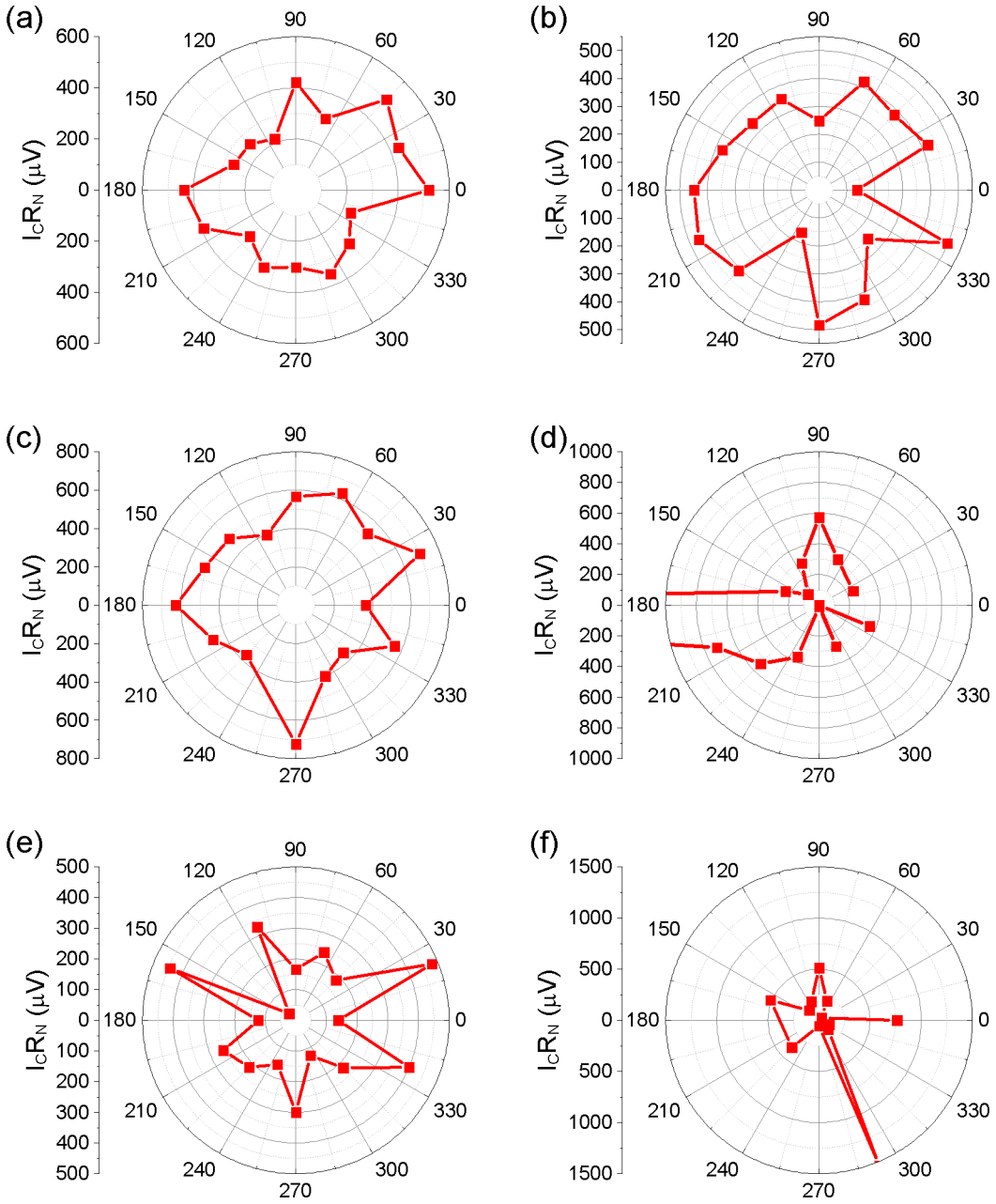

Figure 5.4: The $I_C R_N$ product of (a) 4 μm, (b) 3 μm, (c) 2 μm, (d) 1 μm, (e) 500 nm, and (f) 250 nm wide bridge in different directions.

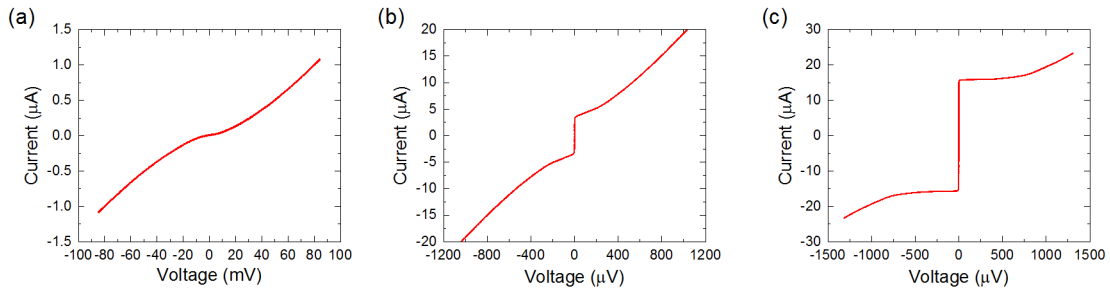

Figure 5.5: I–V of 250 nm-wide junctions at (a) 22.5°, (b) 135°, and (c) 180°. Critical current of the junctions are 0 μA, 4 μA, and 17 μA, respectively.

coefficient of variation which is the standard deviation divided by the mean of $I_C R_N$ for six junctions with different widths. The variation is dramatically increased for junction widths 500 nm and 250 nm, implying that if we are observing the symmetry variations of the order parameter, the grain size of the YBCO film is on the order of few hundred nanometers. Therefore, the larger junction average over many different orientations of grains gives more uniform parameters.

5.4 Conclusion

In conclusion, we have shown the anisotropy of junction parameters potentially indicate the order parameter has $d_{x^2-y^2}$ symmetry. We also made a junction with $I_C R_N$ product of 1 mV. The high $I_C R_N$ value allows a direct interface with semiconductor electronics, more resistant to environmental noise, and stronger signal output. However, the junction size and spacing compared with the grain size are too large to simply probe the order parameter on a single grain since the grain size of the film is probably on the order of the few hundred nanometers. The next step for this experiment is to reduce the size of the junction and/or increase grain size to combine all the junctions to one square. Another modification needed is to increase the resistance and size of the insulating lines to measure the spectroscopy of the junctions at higher bias. Currently, we believe the current path is ill-defined at higher biases, due to higher voltage leakage through the insulating lines. To date, we have promising results as it is still an ongoing goal to probe the in-plane order parameter symmetry.

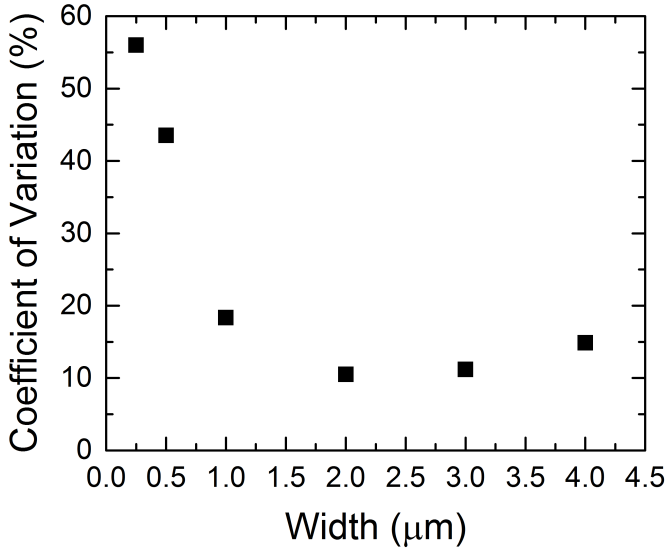

Figure 5.6: The coefficient of variation of the $I_C R_N$ products as a function of junction width.

Chapter 6

Superconducting Quantum Interference Devices

6.1 Motivation

In this chapter we will further examine the noise properties of FHB Josephson junctions. The most common way to determine the noise is through a superconducting quantum interference device (SQUID) [78, 79]. A DC SQUID is two Josephson junctions placed in parallel in a superconducting loop, first invented by R. C. Jaklevic, John Lambe, A.H. Silver, and J. E. Mercereau in 1964 [80]. Figure 6.1 shows a schematic of a SQUID with a bias current and flux Φ in the SQUID loop. Because superconductivity is a coherent phenomenon, the magnetic field penetrating the SQUID loop of area A_{SQ} is the flux ($\Phi = BA_{\mathrm{SQ}}$) causing the interference between the two Josephson junctions. Current through the junctions are $I_1 = \frac{I}{2} - J$ and $I_2 = \frac{I}{2} + J$, where J is the induced current to cancel the applied flux. Also, the resistance of a SQUID (R) is $\frac{1}{R} = \frac{1}{R_{\mathrm{N1}}} + \frac{1}{R_{\mathrm{N2}}}$. This interference is analogous to the Young's double slit interference, where the intensity on the screen of a double slit corresponds to the SQUID critical current or voltage modulation in magnetic field. The only difference is that the intensity in the Young's double slit experiment is the square of the electromagnetic field ($|E^2|$) whereas for a SQUID it is due to a constant

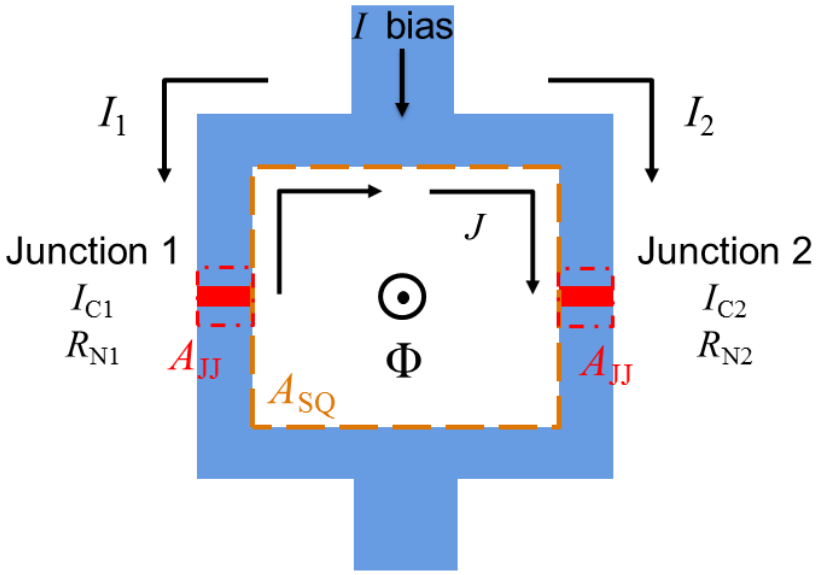

Figure 6.1: A schematic of a SQUID showing the bias current and flux induced circulating current J. The junctions in the SQUID are labeled in red while the dashed squares indicates the SQUID area (orange) and the Josephson junction area (red).

current bias

$$I = I_0 \left| \cos\left(\frac{\pi\Phi}{\Phi_0}\right) \right|, \tag{6.1}$$

where $I_0 = I_{C1} + I_{C2}$ is the total critical current of the SQUID. For the Young's double slit experiment, when the slit width and the slit spacing are comparable, then both diffraction and interference can be observed simultaneously. Similarly, when the junction area (A_{JJ}) is comparable to A_{SQ}, then Eq. (6.1) becomes

$$I = I_0 \left| \mathrm{sinc}\left(\frac{\pi\Phi_{JJ}}{\Phi_0}\right) \cos\left(\frac{\pi\Phi_{SQ}}{\Phi_0}\right) \right|. \tag{6.2}$$

Therefore, a SQUID can measure the magnetic field in units of flux quanta, making it the most sensitive device that measures the magnetic field. As described in chapter 1.1, there are many applications that require an extremely sensitive magnetometer, such as MEG and MCG. Since there is no magnetic monopole, the field strength falls with $\frac{1}{r^3}$ for a dipole source, making the distance between the sensor and the source incredibly crucial. The motivation for a HTS SQUID magnetometer is that the thermal isolation requirements can be greatly reduced, and therefore the sensor can be placed closer to the source. Currently, the best field noise for HTS SQUID

reported was done by Faley *et al.* [81] with step edge junctions. As shown in chapter 1, the junction at the step edge is not a well-defined straight line. To further improve the noise level of a SQUID, FHB junctions could potentially be lower noise than the step edge junction with a well-defined junction barrier.

In addition to biomedical imaging, the field of communications is searching for tera-Hz (THz) sources. Because HTS materials have very large energy gaps that correspond to several THz, this new technology provides new motivation and potential to HTS electronics. In the following experiments, we will present various designs of SQUIDs made with SIS and SNS junctions and their electrical properties.

6.2 Fabrication

Researchers have developed different designs of SQUID for various applications. To increase the magnetic field sensitivity we focus on a particular design where the SQUID is surrounded by a large superconducting plane. Due to the Meissner effect, the magnetic field is focused into the SQUID loop, resulting in a larger effective area with the same external field. This is commonly called a washer SQUID. Figure 6.2 shows a picture of the washer SQUID design that was used in this experiment. The samples were fabricated on 5 mm $\times$ 5 mm substrates with 200 nm Au on 120 nm YBCO from Superconductor Technologies Inc. Using the same process described in chapter 3.2, a 15-turn coil and a 1 mm^2 washer SQUID was patterned with photolithography and Ar^+ milling. The center of the SQUID was thinned to approximately 30 nm, exposing the 4×14 μm^2 SQUID loop. Lastly, the junctions were irradiated with lines 200 ions/nm and 450 ions/nm on 4 μm wide bridges in the thinned-down window (Fig. 6.2(b)). The field sensitivity of the SQUID depends on flux noise of the SQUID and the SQUID period. To increase the SQUID period, a multiturn flux transformer is usually integrated with the SQUID [82]. A second design of washer SQUIDs was built to add a flux transformer. Due to the complex processing required to make multilayer cross over links for a flux transformer, this design allows us to adapt flux transformer chips to this SQUID. Figure 6.3 shows an optical picture of a multiturn flux transformer by Faley *et al.* flip chipped (upside down) on top of a washer SQUID. The junctions were written with 300 ions/nm.

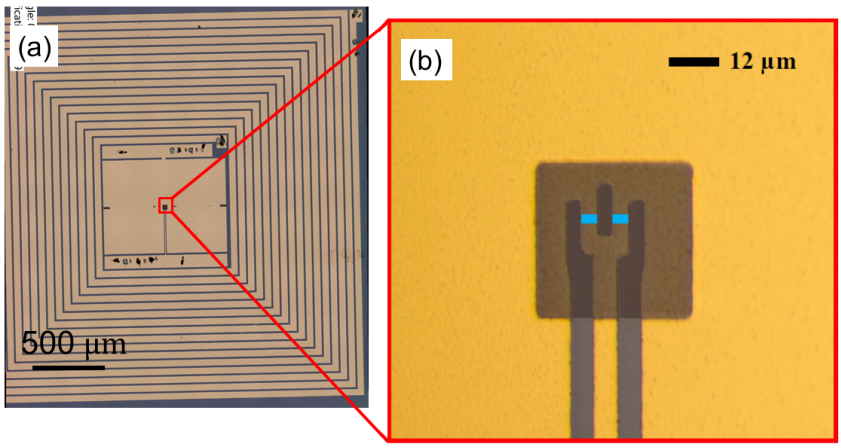

Figure 6.2: A picture of the sample SQUID, that consists of a 1 mm square washer around the 4×14 μm^2 SQUID loop. The junctions in the SQUID are 4 μm wide and were irradiated with 200 ions/nm and 450 ions/nm, indicated with two blue lines. A 15-turn on-chip coil surrounds the washer.

6.3 Measurements and results

Figure 6.4 shows basic DC measurements of an SIS SQUID shown in blue and an SNS SQUID shown in red, which were measured at 4 K and 50 K, respectively. The I_0R product from the I–V characteristics of the SIS SQUID and SNS SQUID, which exhibit the characteristics of an RSJ model, are 270 μV and 60 μV, respectively. The resistance of an individual SIS junction (twice the SQUID resistance) is approximately 25 Ω, following the similar argument in chapter 3 and 4 that the junction is in the overdamped regime ($\beta_C = 0.032 << 1$). Although in Eq. (6.1) and (6.2) the SQUID modulation in magnetic field is presented as critical current, in practice and applications, the SQUID is biased with a constant current slightly higher than I_0 and the voltage variation with applied B-field is measured. Figure 6.4 (c), (d), (e), and (f) illustrate the voltage-magnetic field characteristics (V–B) of SIS and SNS SQUIDs in different field ranges. The SQUID period shown in figure 6.4(c) and 6.4(d) of the SIS and SNS SQUIDs are 1 μT and the voltage modulation amplitudes are 200 μV and 25 μV, respectively. Lastly, figure 6.4(e) and 6.4(f) are V–B at a larger field range to show both the SQUID oscillations and the junction Fraunhofer pattern. The first minimum of the junction pattern occurs at 25 μT for SIS and SNS SQUIDs, meanwhile, the second minimum occurs at 50 μT and 70 μT, respectively.

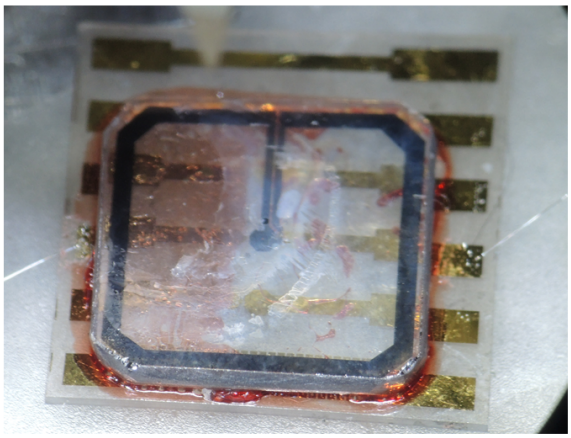

Figure 6.3: A picture of a washer squid with a flux transformer by Faley *et al.* on top.

The SIS SQUID was also measured out to higher current and voltage bias to show the quasiparticle transport. Figure 6.5 shows I–V and the dynamic conductance $\frac{dV}{dI}$ biased out to 60 mV. The I–V has typical SIS characteristics, and a peak in $\frac{dV}{dI}$ occurs at 20 mV. Using the second design shown in figure 6.3, we measured the noise of the SQUID at 68 K with Tristan Technologies iMAG® flux locked loop. A flux locked loop is a feedback system that keeps the optimal field bias [83]. The output of the flux lock loop was connected to a spectrum analyzer, with results shown in figure 6.6. The voltage white noise level of the FHB SNS SQUID is slightly above 10 $\mu\Phi_0/\mathrm{Hz}^{-1/2}$, and at 10 Hz the noise is less than 20 $\mu\Phi_0/\mathrm{Hz}^{-1/2}$. As a comparison, a step edge junction SQUID by Faley *et al.* has white noise of 10 $\mu\Phi_0/\mathrm{Hz}^{-1/2}$ at 1000 Hz and 20 $\mu\Phi_0/\mathrm{Hz}^{-1/2}$ at 10 Hz measured at 77 K [82, 81]. The flux noise was back calculated from the magnetic field noise using the flux sensitivity of 1 nT/Φ_0 of the flux transformer. The difference starts to appear at frequencies less than 10 Hz. At 1 Hz, the FHB SQUID has a noise level of 20 $\mu\Phi_0/\mathrm{Hz}^{-1/2}$ whereas the bicrystal junction is at 50 $\mu\Phi_0/\mathrm{Hz}^{-1/2}$. A typical commercial LTS SQUID noise is also shown in the figure as a reference.

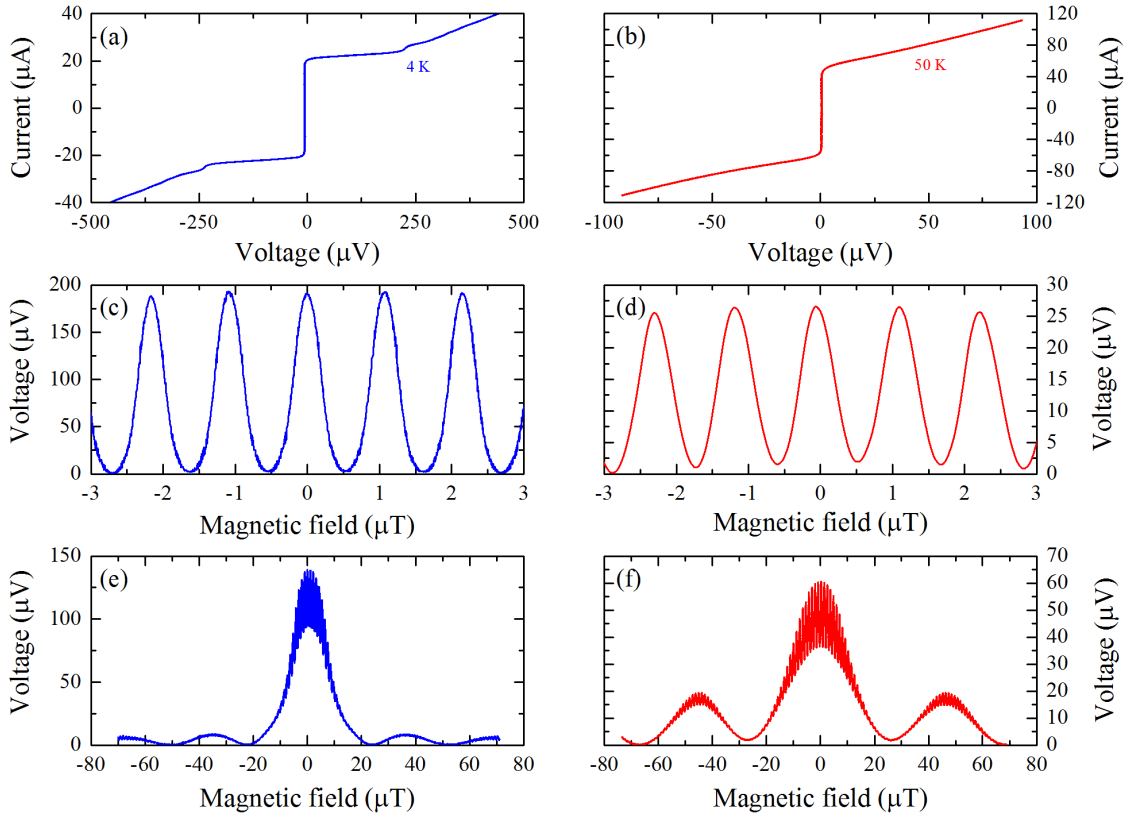

Figure 6.4: DC measurements of SIS SQUID shown in blue at 4 K and SNS SQUID shown in red measured at 50 K. Current-voltage characteristics of (a) SIS and (b) SNS SQUIDs. Voltage-magnetic field characteristics of (c) SIS and (d) SNS SQUIDs showing the voltage modulation at a constant current bias. Higher magnetic field range sweep showing the Fraunhofer pattern of the junctions in the (e) SIS and (f) SNS SQUIDs. The voltages from the magnetic field measurements were shifted to zero for clarity. (c) and (e) are measured out to higher field ranges; note the modulation voltage is reduced for larger field ranges.

6.4 Discussions

From the data presented in this chapter, the FHB SQUIDs show large voltage modulations in V–B that are comparable to the I_0R of the SQUID. The parameter that determines the modulation depth in V–B is $\beta_L = \frac{LI_0}{\Phi_0}$ [78, 84]. In this experiment, SIS SQUID has a $\beta_L << 1$ since the voltage almost fully modulates to zero, while the SNS SQUID has a $\beta_L \sim 1$ for 50% modulation. However, it is difficult to predict or "engineer" β_L due to the kinetic inductance of ultra thin films. When the film thickness is less than the penetration depth λ_L, λ_L needs to be modified to

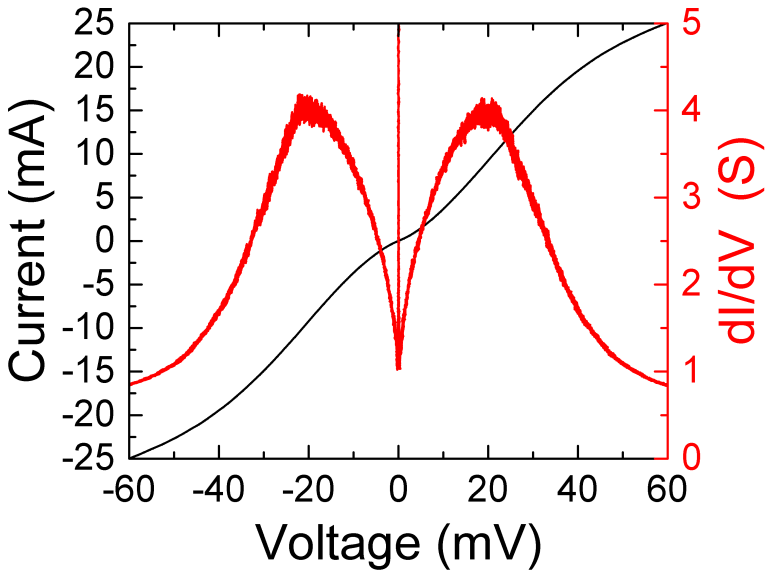

Figure 6.5: I–V (black) and the dynamic conductance (red) of the SIS SQUID measured at high bias. The peak of the dynamic conductance occurs at approximately 20 mV.

$\lambda_\perp = \frac{\lambda_L^2}{t}$. As a result, the kinetic inductance becomes much greater than the geometric inductance. For the SIS SQUID, the gap-like feature occurs at a different peak value (at 20 mV) than the example presented in chapter 3. We believe the difference is due to different starting materials: both peak values fall within the values reported in the literature. The flux noise of a SQUID represents the quality of the SQUID. Our FHB SQUID matched the same noise level as the current state-of-the-art HTS SQUID in the high frequency range(white noise f^0), and out-performed it at lower frequency (pink noise $\frac{1}{f}$) than 10 Hz. Most biomedical signals are less than 10 Hz, where the FHB SQUID has less $\frac{1}{f}$ noise and out performs the step edge SQUID. In practice, the SQUID has to be able to detect magnetic field from the source. Therefore, the magnetic field noise is the criterion. In work by Faley *et al.* [81], the step edge SQUID sensor can reach 7 fT/Hz$^{-1/2}$ at 10 Hz, while the LTS SQUID sensor noise level is 5 fT/Hz$^{-1/2}$. The magnetic field noise level can be reduced by a flux transformer to reduce the SQUID period. By combining an inductance-matched flux transformer with a FHB SQUID, there is the very real potential of surpassing the signal-to-noise ratio of the LTS SQUID sensor.

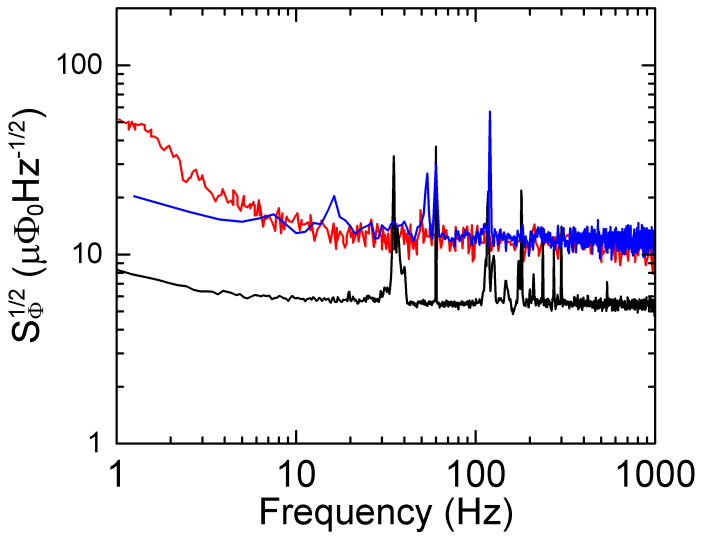

Figure 6.6: A comparison of the flux noise spectrum for SQUIDs fabricated with different technologies. The blue is the FHB SQUID measured at 68 K and the red is the SQUID by Faley *et al.* measured at 77 K. A LTS commercial SQUID from Tristan Technologies Inc. measured at 4 K is shown in black as a reference.

6.5 Conclusion

In conclusion, we have demonstrated YBCO SQUIDs fabricated with a focused helium beam with both SIS and SNS junctions. The FHB SQUIDs exhibit higher voltage modulation in field than the masked junction SQUIDs and are comparable to other technologies. Furthermore, the voltage modulation can reach the I_0R product determined from I–V characteristics. Both SNS and SIS SQUIDs have RSJ-like I–V characteristics for low bias. At high bias, the I–V of SIS SQUID also exhibits typical tunneling characteristics and gap-like features in the dynamic conductance. Currently, the magnetic field noise of the state-of-the-art HTS SQUIDs are comparable to the LTS SQUID at 77 K. FHB SQUIDs have similar or even better intrinsic flux noise than that of current state-of-the-art HTS SQUIDs. In addition, FHB SQUIDs have very simple fabrication processes and high yields, which solve the current major roadblock for the HTS SQUIDs. Furthermore, the noise of the FHB SQUIDs can be further improved with the nanojunctions [85] mentioned in chapter 4. The future is bright for different applications of HTS SQUIDs.

6.6 Acknowledgement

Chapter 6, in part, has been submitted for publication of the material as it may appear in *Applied Physics Letters*, 2015, E. Y. Cho, M. K. Ma, C. Huynh, K. Pratt, D. N. Paulson, V. N. Glyantsev, R. C. Dynes, and S. A. Cybart, American Institute of Physics, 2015. The dissertation author was the primary investigator and author of this paper.

Chapter 7

Junction arrays

7.1 Motivation

In many applications of Josephson junctions and SQUIDs, higher output voltage, larger dynamic range, or impedance matching devices are required for example in communications [86, 16] and digital circuits [13, 15]. Since the voltage output adds linearly with number of SQUIDs in series (N), and while critical current scales with number of SQUIDs in each parallel segment (M). The resistance of a $N \times M$ array scales as $R_{\text{array}} = \frac{N}{M}R$. Array of SQUIDs provides the possibility of satisfying most of the requirements [46, 58]. In addition, it is commonly believed that the noise of an array increases as$\sqrt{N}$, along with the scaling of voltage with N, and so the signal-to-noise ratio could improve as $\frac{N}{\sqrt{N}} = \sqrt{N}$. Another potential design is a 1D array of long junctions. A long junction is when the width of the junction is greater than the Josephson penetration depth λ_{J} as described in chapter 1. Figure 7.1 shows the evolution of the $I_{\text{C}}(B)$ as the junction width changes from (a) five times λ_{J} to (d) two times λ_{J}. Due to the self-field effect from the applied measuring current, the magnetic field response is skewed making the resultant Fraunhofer pattern more triangular and tilted. Eventually with increasing width the V–B becomes a multivalued function and the minima disappear [34, 87]. $I_{\text{C}}(B)$ in principle can be converted to V–B with the normal state resistance. If the width of the junction is chosen properly, in theory, the slope of the transfer function can approach infinity, for example, in figure 7.1(b). Therefore, with this vertical $I_{\text{C}}(B)$ a device could be current and magnetic field biased

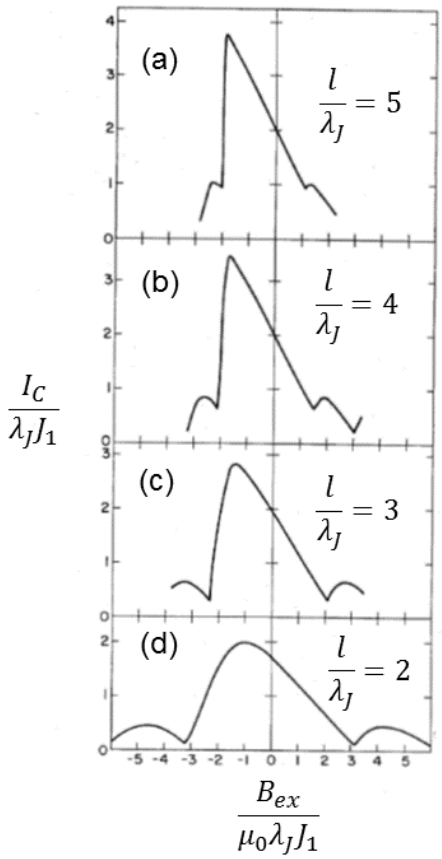

Figure 7.1: Figure adapted from Basavaiah *et al.* [87] showing the $I_C(B)$s for different bridge width.

at the most sensitive part of the V–B for maximum performance. The sensitivity of a 1D array of long junctions (or Fraunhofer amplifier) can approach the sensitivity of a SQUID with much larger dynamic range. In addition, the SQUID oscillations that follow Eq. (6.1) and Eq. (6.2) are not linear functions. On the other hand, from [34], a portion of the center peak of V–B for a long junction is linear. In this chapter, we will demonstrate both designs.

7.2 SQUID arrays

A test sample was fabricated on a 25 nm-thick YBCO film on Sapphire covered with 200 nm of gold. Using the same processes as described in chapter 3.2 for the

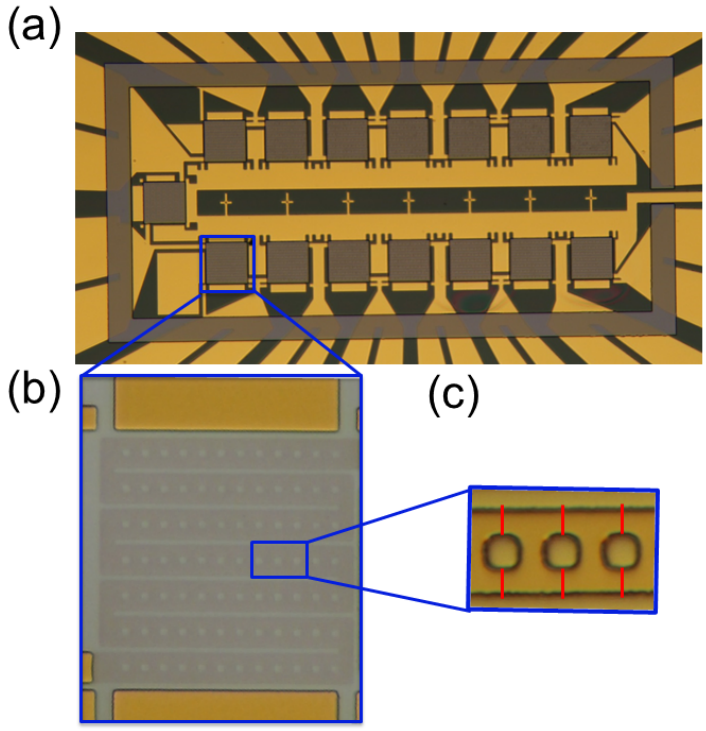

Figure 7.2: Optical pictures of the 1D SQUID array sample at different magnifications. The sample has 15 cells with each cell (b) having 84 SQUIDs in series and each SQUID has a 5 μm $\times$ 5 μm loop with a 4 micron wide bridge. The junctions were labeled with red lines in (c).

thinner YBCO films. Due to limitations of the helium ion microscope, the SQUID array was separated into a series of 15 cells of 100-micron wide write fields as shown in figure 7.2(a). In each cell there are 84 SQUIDs in series (Fig. 7.2(b)) in a meander line. Each cell has independent voltage probes that allow 4-point measurements on the whole array, partial array, or individual cells. Each SQUID has a 5 μm $\times$ 5 μm loop and 4 micron wide bridges. The junctions in each SQUID were written with 300 ions/nm as shown in red lines in figure 7.2(c).

The sample was measured in a pumped liquid nitrogen cryostat cooled below 77 K [88]. Figure 7.3(a) shows the IV of a single cell in the sample, the resistance of the array is approximately 140 Ω and the critical current is approximately 20 μA at 51.6 K. The *V–B* shown in figure 7.3(b) for 14 cells in series, 1176 SQUIDs, has voltage modulation of 2.5 mV with magnetic field period of 30 μT at 65 K. The transfer function of the device with 1176 SQUIDs is approximately 160 V/T. As a

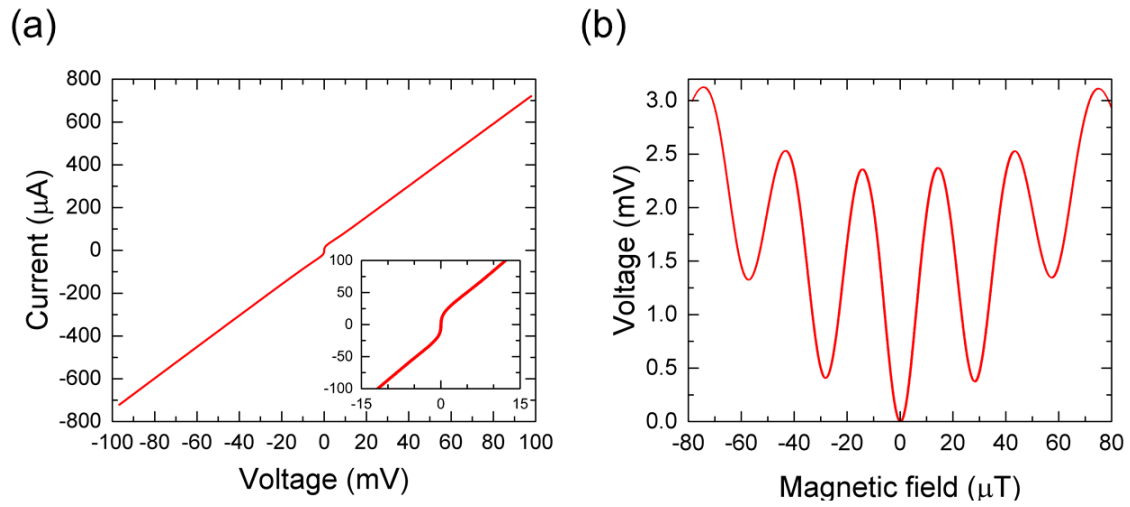

Figure 7.3: (a) I–V of a single cell of 84 SQUIDs measured at 51.6 K, the inset shows a zoomed-in curve of the same I–V near zero bias. (b) V–B of 14 cells in series at 65 K, a total of 1176 SQUIDs. Maximum voltage modulation is approximately 2.5 mV.

comparison in [58] the transfer function of 5225×6 array is 500 V/T at 34 K.

7.3 Single junction arrays

The designs of single junction arrays are very straightforward, a 1 mm-long bridge of 10 μm and 20 μm width with four contact pads for 4-point measurements. As described in chapter 3.2, the samples were fabricated with the same processes. The 1 mm long bridge was separated into eight 150 μm-wide write fields and the 10 micron-wide array was irradiated with 350 ions/nm while the 20 micron-wide array was with 200 ions/nm. Both arrays have 600 junctions in series and were tested in a cryocooler. Figure 7.4 illustrates the I–V (a) and V–B (b) of the 10 micron-wide array. This device has a critical current of $\sim$ 120 μA and a resistance of $\sim$ 90 Ω at 61 K. The maximum voltage modulation of 23 mV in V–B is shown in the inset of figure 7.4(b), where the most linear part has a transfer function of 500 V/T and dynamic range over approximately 30 μT and 12 mV. The field range in figure 7.4(b) is offset in B due the field generated by the bias current and the Bean effect [89, 90], when the current applies a Lorentz force on the fluxoid. Hence, the V–B becomes

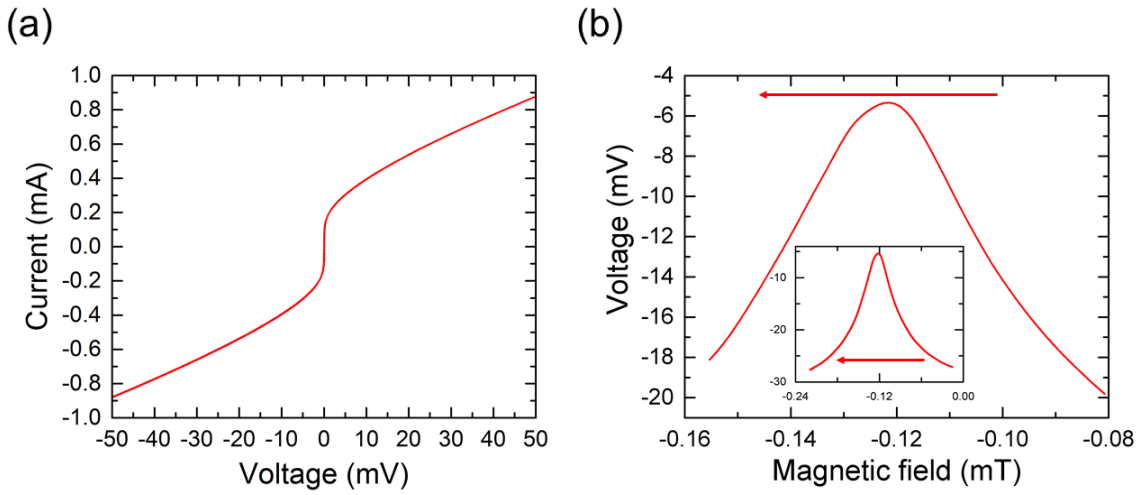

Figure 7.4: (a)I–V of six hundred 10 micron wide junctions in series measured at 61 K. (b) The linear part of the V–B of the 10 micron wide array measured at 60.5 K, where the red arrow indicates the magnetic field sweep direction. The inset of (b) is the V–B measured at a larger field range.

hysteretic in figure 7.4(b) and only a curve measured sweeping field in one direction was shown to emphasize the transfer function. Similarly, the I–V and V–B of the 20 micron-wide array are shown in figure 7.5(a) and 7.5(b), respectively. The array has R_{N} of 35 Ω and I_{C} of 1.2 mA at 73 K. Due to the larger bridge width the V–B is tilted much more than the 20 micron-wide array, with a transfer function of 27 V/T.

7.4 Conclusion

In this chapter, we presented both single junction arrays and single SQUID arrays. Although SQUID arrays have larger dynamic range and more tunable I_{C} and R_{N}, a flux transformer on a washer SQUID still provides higher sensitivity. In order for a typical SQUID array with a voltage modulation of 2.5 mV and a SQUID period of 30 μT to match a 100 μV, 1 nT washer SQUID with a flux transformer, the array has to be over three orders of magnitude larger. Further analysis and discussion of the SQUID arrays is done in the thesis of Travis J. Wong [88]. The long junction arrays have very large dynamic range compared to a SQUID array and can operate in non-zero magnetic field. In addition, from the skewness of the two arrays, the

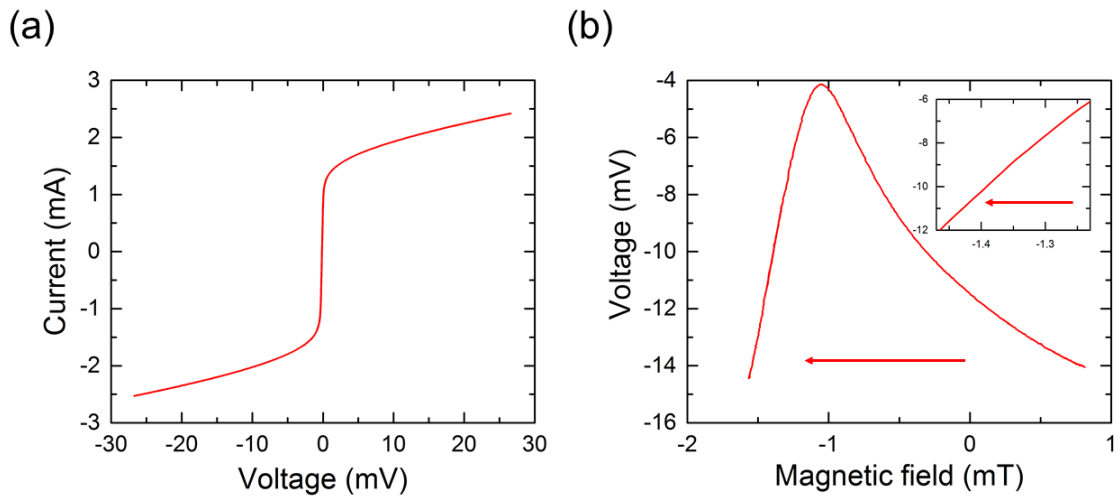

Figure 7.5: (a) I–V of six hundred 20 micron wide junctions in series measured at 73 K. (b) V–B of the 20 micron wide array measured at 73 K, where the red arrow indicates the magnetic field sweep direction. The inset of (b) zooms in to the steeper half of the V–B peak.

sensitivity depends heavily on the bridge width. Trimming the bridges with FHB could potentially increase the uniformity of the arrays.

Chapter 8

Conclusion

In this thesis, I have experimentally developed an expectation that came from our group investigations. The belief was based on our previous work on masked ion irradiated Josephson junctions and the BTK theory. By reducing the barrier width and increasing the strength of the barrier, the junctions should undergo a metal-insulator transition. Previously, the mask feature size and the irradiation damage profile were too large for quasiparticle tunneling. With the newly developed focused helium ion beam microscope by Carl Zeiss Microscopy$^{\text{TM}}$, it is possible to pattern at much smaller length scale. I observed a continuous change in the electrical properties of the junction barrier, from metallic to insulating, by varying only the irradiation dose to control the barrier strength. With FHB SIS junctions, I performed in-plane tunneling spectroscopy of YBCO-YBCO junctions for the first time, confirming the gap-like feature and peak dynamic conductance. The temperature dependence of the peak dynamic conductance fitted very well with the BCS theory. Furthermore, I observed hints of the angular dependence of $I_{\text{C}}R_{\text{N}}$ when placed at different orientations with respect to the crystal.

In addition to patterning the junction, an FHB can also be used to pattern the circuit using higher dose to drive YBCO insulating, therefore, defining a current path. Patterning circuits with an FHB can easily exceed the limitations of current fabrication processes that will damage the materials. I have shown junctions as small as 20 nm wide on a 25 nm-thick film. This technique opens up a large parameter space where I_{C}, R_{N}, β_{C}, and temperature dependence can be individually tuned with dose,

junction orientation, and bridge size. The SQUID made with FHB junctions exhibits large voltage modulation that is close to the I_0R_N, and the flux noise level is on par with current state-of-the-art HTS SQUIDs at high frequencies and better below 10 Hz. Arrays of FHB SQUIDs and array of single junctions have suggested uniformity better than the previous masked ion irradiation junctions. A current engineering obstacle in HTS electronics is the lack of a reliable large scale process to reduce the cost of each device. The direct-write processing greatly simplifies the fabrication of HTS circuits and has the potential of wafer scale processing. This technique is not unique to YBCO but to all materials that are sensitive to disorder. For example, I have made FHB Josephson junctions in both iron-based superconductor (Co-FeAs) and MgB_2, as well as modifying the conductance in semiconductor (GeAs).

Despite the advancements in focused ion beam technology and the exciting results from the FHB microscope, there is still huge improvement needed for this technology to be mature. Currently, the beam energy is limited to 30 keV because the FHB was designed to be used as a microscope. This limitation restricts the maximum film thickness, such that the penetration depth $\lambda_\perp$ is long and the kinetic inductance is very high. Higher beam energy would allow the processing of thicker films with better superconducting properties, potentially renewing the interest in HTS electronics for biomedical imaging, digital circuits, and quantum computing. Most importantly, higher energy beams could have smaller beam size and narrower barriers for true tunneling junctions without hopping transport. By doing so, physicists can potentially study the superconducting mechanism behind the unconventional superconductors and make significant strides towards solving the great mystery that has puzzled physicists for 30 years since the discovery of HTS in 1986.

Bibliography

[1] R.M Leahy, J.C Mosher, M.E Spencer, M.X Huang, and J.D Lewine. A study of dipole localization accuracy for MEG and EEG using a human skull phantom. *Electroencephalography and Clinical Neurophysiology*, 107(2):159–173, 1998.

[2] M X Huang, J C Mosher, R M Leahy, Cuffin B N, Zhang X Ferguson A S, Stroink G, Geselowitz D B, Geselowitz D B, Golub G H F, Van Loan C, Hmlinen M S J, Sarvas, Supek S Best E Ranken D Huang M, Aine C J, Flynn E R, Hmlinen M S Ilmoniemi R J, Knuutila J, Spencer M E Huang M X Leahy R M, Mosher J C, Lewine J D, Peters M J Meijs J W H, Bosch F G C, Lopes da Silva F H, Leahy R M Mosher J C, Lewis P S, Lewis P S Mosher J C, Leahy R M, Leahy R M Mosher J C, Spencer M E, Lewis P S, Nelder J A R, Mead, Ranken D J, George, Sarvas J, Aaron R Best E Schlitt H, Heller L, Ranken D, Best E Ranken D Schlitt H, Heller L, and Aaron R. A sensor-weighted overlapping-sphere head model and exhaustive head model comparison for MEG. *Physics in Medicine and Biology*, 44(2):423–440, 2 1999.

[3] D Cohen. Magnetoencephalography: evidence of magnetic fields produced by alpha-rhythm currents. *Science (New York, N.Y.)*, 161(3843):784–6, 8 1968.

[4] Hans Koch. Recent advances in magnetocardiography. *Journal of Electrocardiology*, 37:117–122, 2004.

[5] Werner Moshage, Stephan Achenbach, Konrad Göhl, and Kurt Bachmann. Evaluation of the non-invasive localization accuracy of cardiac arrhythmias attainable by multichannel magnetocardiography (MCG). *The International Journal of Cardiac Imaging*, 12(1):47–59, 3 1996.

[6] Kenji Nakai, Kohei Kawazoe, Hiroshi Izumoto, Junichi Tsuboi, Yu Oshima, Takanori Oka, Kunihiro Yoshioka, Masanori Shozushima, Akira Suwabe, Manabu Itoh, Koichiro Kobayashi, Takayuki Shimizu, and Masahito Yoshizawa. Construction of a Three-dimensional Outline of the Heart and Conduction Pathway by Means of a 64-channel Magnetocardiogram in Patients with Atrial Flutter and Fibrillation. *The International Journal of Cardiovascular Imaging*, 21(5):555–561, 10 2005.

[7] Kirsten Tolstrup, Bo E. Madsen, Jose A. Ruiz, Stephen D. Greenwood, Judeen Camacho, Robert J. Siegel, H. Caroline Gertzen, Jai-Wun Park, and Peter A. Smars. Non-Invasive Resting Magnetocardiographic Imaging for the Rapid Detection of Ischemia in Subjects Presenting with Chest Pain. *Cardiology*, 106(4):270–276, 11 2006.

[8] T.H. Buttgenbach, H.G. LeDuc, P.D. Maker, and T.G. Phillips. A fixed tuned broadband matching structure for submillimeter SIS receivers. *IEEE Transactions on Appiled Superconductivity*, 2(3):165–175, 1992.

[9] N. Oukhanski, R. Stolz, V. Zakosarenko, and H.-G. Meyer. Low-drift broadband directly coupled dc SQUID read-out electronics. *Physica C: Superconductivity*, 368(1):166–170, 2002.

[10] V. K. Kornev, I. I. Soloviev, A. V. Sharafiev, N. V. Klenov, and O. A. Mukhanov. Active Electrically Small Antenna Based on Superconducting Quantum Array. *IEEE Transactions on Applied Superconductivity*, 23(3):1800405–1800405, 6 2013.

[11] S. Shokhor, B. Nadgorny, M. Gurvitch, V. Semenov, Yu. Polyakov, K. Likharev, S. Y. Hou, and Julia M. Phillips. All-high-Tc superconductor rapid-single-flux-quantum circuit operating at 30 K. *Applied Physics Letters*, 67(19):2869, 11 1995.

[12] PAUL BUNYK, KONSTANTIN LIKHAREV, and DMITRY ZINOVIEV. RSFQ TECHNOLOGY: PHYSICS AND DEVICES. *International Journal of High Speed Electronics and Systems*, 11(01):257–305, 3 2001.

[13] K.K. Likharev and V.K. Semenov. RSFQ logic/memory family: a new Josephson-junction technology for sub-terahertz-clock-frequency digital systems. *IEEE Transactions on Appiled Superconductivity*, 1(1):3–28, 3 1991.

[14] R. McDermott and M.G. Vavilov. Accurate Qubit Control with Single Flux Quantum Pulses. *Physical Review Applied*, 2(1):014007, 7 2014.

[15] John X. Przybysz, Donald L. Miller, Hannes Toepfer, Oleg Mukhanov, Jrgen Lisenfeld, Martin Weides, Hannes Rotzinger, and Pascal Febvre. Superconductor Digital Electronics. In *Applied Superconductivity*, pages 1111–1206. Wiley-VCH Verlag GmbH & Co. KGaA, Weinheim, Germany, 1 2015.

[16] Sergey K. Tolpygo. Superconductor digital electronics: Scalability and energy efficiency issues (Review Article). *Low Temperature Physics*, 42(5):361–379, 5 2016.

[17] C.P. Foley, K.E. Leslie, R. Binks, C. Lewis, W. Murray, G.J. Sloggett, S. Lam, B. Sankrithyan, N. Savvides, A. Katzaros, K.-H. Muller, E.E. Mitchell, J. Pollock, J. Lee, D.L. Dart, R.R. Barrow, M. Asten, A. Maddever, G. Panjkovic,

M. Downey, C. Hoffman, and R. Turner. Field trials using HTS SQUID magnetometers for ground-based and airborne geophysical applications. *IEEE Transactions on Appiled Superconductivity*, 9(2):3786–3792, 6 1999.

[18] S. P. Benz and C. A. Hamilton. A pulse-driven programmable Josephson voltage standard. *Applied Physics Letters*, 68(22):3171, 1996.

[19] Clark A. Hamilton. Josephson voltage standards. *Review of Scientific Instruments*, 71(10):3611, 2000.

[20] John C. Mather. Bolometer noise: nonequilibrium theory. *Applied Optics*, 21(6):1125, 3 1982.

[21] John Ruhl, Peter A. R. Ade, John E. Carlstrom, Hsiao-Mei Cho, Thomas Crawford, Matt Dobbs, Chris H. Greer, Nils w. Halverson, William L. Holzapfel, Trevor M. Lanting, Adrian T. Lee, Erik M. Leitch, Jon Leong, Wenyang Lu, Martin Lueker, Jared Mehl, Stephan S. Meyer, Joe J. Mohr, Steve Padin, T. Plagge, Clem Pryke, Marcus C. Runyan, Dan Schwan, M. K. Sharp, Helmuth Spieler, Zak Staniszewski, and Antony A. Stark. The South Pole Telescope. pages 11–29. International Society for Optics and Photonics, 10 2004.

[22] Erik Lucero, R. Barends, Y. Chen, J. Kelly, M. Mariantoni, A. Megrant, P. OMalley, D. Sank, A. Vainsencher, J. Wenner, T. White, Y. Yin, A. N. Cleland, and John M. Martinis. Computing prime factors with a Josephson phase qubit quantum processor. *Nature Physics*, 8(10):719–723, 8 2012.

[23] R. Barends, J. Kelly, A. Megrant, A. Veitia, D. Sank, E. Jeffrey, T. C. White, J. Mutus, A. G. Fowler, B. Campbell, Y. Chen, Z. Chen, B. Chiaro, A. Dunsworth, C. Neill, P. OMalley, P. Roushan, A. Vainsencher, J. Wenner, A. N. Korotkov, A. N. Cleland, and John M. Martinis. Superconducting quantum circuits at the surface code threshold for fault tolerance. *Nature*, 508(7497):500–503, 4 2014.

[24] Andrew A. Houck, Hakan E. Türeci, and Jens Koch. On-chip quantum simulation with superconducting circuits. *Nature Physics*, 8(4):292–299, 4 2012.

[25] Z. Kim, V. Zaretskey, Y. Yoon, J. F. Schneiderman, M. D. Shaw, P. M. Echternach, F. C. Wellstood, and B. S. Palmer. Anomalous avoided level crossings in a Cooper-pair box spectrum. *Physical Review B*, 78(14):144506, 10 2008.

[26] Matteo Mariantoni, H Wang, T Yamamoto, M Neeley, Radoslaw C Bialczak, Y Chen, M Lenander, Erik Lucero, A D O'Connell, D Sank, M Weides, J Wenner, Y Yin, J Zhao, A N Korotkov, A N Cleland, John M Martinis, D. P. DiVincenzo, L. M. K. Vandersypen, D. G. Cory, Y. S. Weinstein, M. A. Pravia, E. M. Fortunato, S. Lloyd, D. G. Cory, R. Blatt, D. Wineland, J. Chiaverini, T. Monz, D. J. Reilly, B. P. Lanyon, K. S. Choi, H. Deng, J. Laurat, H. J.

Kimble, J. Clarke, F. K. Wilhelm, J. H. Plantenberg, P. C. de Groot, C. J. P. M. Harmans, J. E. Mooij, L. DiCarlo, P. J. Leek, T. Yamamoto, M. Neeley, L. Dicarlo, M. Mariantoni, H. Wang, M. D. Reed, R. Horodecki, P. Horodecki, M. Horodecki, K. Horodecki, F. W. Strauch, A. Barenco, T. C. Ralph, K. J. Resch, and A. Gilchrist. Implementing the quantum von Neumann architecture with superconducting circuits. *Science (New York, N.Y.)*, 334(6052):61–5, 10 2011.

[27] Matthew Neeley, M. Ansmann, Radoslaw C. Bialczak, M. Hofheinz, N. Katz, Erik Lucero, A. OConnell, H. Wang, A. N. Cleland, and John M. Martinis. Process tomography of quantum memory in a Josephson-phase qubit coupled to a two-level state. *Nature Physics*, 4(7):523–526, 7 2008.

[28] S. Novikov, J. E. Robinson, Z. K. Keane, B. Suri, F. C. Wellstood, and B. S. Palmer. Autler-Townes splitting in a three-dimensional transmon superconducting qubit. *Physical Review B*, 88(6):060503, 8 2013.

[29] K. D. Petersson, L. W. McFaul, M. D. Schroer, M. Jung, J. M. Taylor, A. A. Houck, and J. R. Petta. Circuit quantum electrodynamics with a spin qubit. *Nature*, 490(7420):380–383, 10 2012.

[30] B.D. Josephson. Possible new effects in superconductive tunnelling. *Physics Letters*, 1(7):251–253, 7 1962.

[31] J. Bardeen, L. N. Cooper, and J. R. Schrieffer. Theory of superconductivity. *Physical Review*, 108(5):1175–1204, 12 1957.

[32] P. W. Anderson and J. M. Rowell. Probable Observation of the Josephson Superconducting Tunneling Effect. *Physical Review Letters*, 10(6):230–232, 3 1963.

[33] Sidney Shapiro. Microwave Harmonic Generation from Josephson Junctions. *Journal of Applied Physics*, 38(4):1879, 6 1967.

[34] C. S. Owen and D. J. Scalapino. Vortex Structure and Critical Currents in Josephson Junctions. *Physical Review*, 164(2):538–544, 12 1967.

[35] W. C. Stewart. CURRENT-VOLTAGE CHARACTERISTICS OF JOSEPHSON JUNCTIONS. *Applied Physics Letters*, 12(8):277, 10 1968.

[36] D. E. McCumber. Effect of ac Impedance on dc Voltage-Current Characteristics of Superconductor Weak-Link Junctions. *Journal of Applied Physics*, 39(7):3113, 11 1968.

[37] T.A. Fulton, R.C. Dynes, and P.W. Anderson. The flux shuttleA Josephson junction shift register employing single flux quanta. *Proceedings of the IEEE*, 61(1):28–35, 1973.

[38] J. G. Bednorz and K. A. Muller. Possible highT c superconductivity in the Ba-La-Cu-O system. *Zeitschrift fur Physik B Condensed Matter*, 64(2):189–193, 6 1986.

[39] M. K. Wu, J. R. Ashburn, C. J. Torng, P. H. Hor, R. L. Meng, L. Gao, Z. J. Huang, Y. Q. Wang, and C. W. Chu. Superconductivity at 93 K in a new mixed-phase Y-Ba-Cu-O compound system at ambient pressure. *Physical Review Letters*, 58(9):908–910, 3 1987.

[40] Jin-Tae Kim, J. Giapintzakis, and D. M. Ginsberg. Anisotropy of the resistivity in thea?b plane of a superconducting YBa2Cu3O7 ??single crystal. *Journal of Superconductivity*, 9(5):481–484, 10 1996.

[41] A. S. Katz, A. G. Sun, S. I. Woods, and R. C. Dynes. Planar thin film YBa[sub 2]Cu[sub 3]O[sub 7δ] Josephson junctions via nanolithography and ion damage. *Applied Physics Letters*, 72(16):2032, 1998.

[42] S. Tolpygo, B. Nadgorny, S. Shokhor, F. Tafuri, Y. Lin, A. Bourdillon, and M. Gurvitch. Electron beam writing in fabricating planar high-Tc Josephson junctions. *Physica C: Superconductivity*, 209(1-3):211–214, 4 1993.

[43] B. A. Davidson, J. E. Nordman, B. M. Hinaus, M. S. Rzchowski, K. Siangchaew, and M. Libera. Superconductor-normal-superconductor behavior of Josephson junctions scribed in Y1Ba2Cu3O7δ by a high-brightness electron source. *Applied Physics Letters*, 68(26):3811, 1996.

[44] A. J. Pauza, W. E. Booij, K. Herrmann, D. F. Moore, M. G. Blamire, D. A. Rudman, and L. R. Vale. Electron-beam damaged high-temperature superconductor Josephson junctions. *Journal of Applied Physics*, 82(11):5612, 1997.

[45] W. E. Booij, A. J. Pauza, E. J. Tarte, D. F. Moore, and M. G. Blamire. Proximity coupling in high- T c Josephson junctions produced by focused electron beam irradiation. *Physical Review B*, 55(21):14600–14609, 6 1997.

[46] Shane A. Cybart, Steven M. Anton, Stephen M. Wu, John Clarke, and Robert C. Dynes. Very Large Scale Integration of Nanopatterned YBa 2 Cu 3 O 7δ Josephson Junctions in a Two-Dimensional Array. *Nano Letters*, 9(10):3581–3585, 10 2009.

[47] SK Bahl, N Bluzer, and RE Glover. In-situ optical properties of amorphous ge films deposited at 4.2 k. In *BULLETIN OF THE AMERICAN PHYSICAL SOCIETY*, volume 18, pages 132–132. AMER INST PHYSICS CIRCULATION FULFILLMENT DIV, 500 SUNNYSIDE BLVD, WOODBURY, NY 11797-2999, 1973.

[48] L. Merchant, J. Ostrick, R. P. Barber, and R. C. Dynes. Crossover from phase fluctuation to amplitude-dominated superconductivity: A model system. *Physical Review B*, 63(13):134508, 3 2001.

[49] P. Xiong, A. V. Herzog, and R. C. Dynes. Superconductivity in ultrathin quench-condensed Pb/Sb and Pb/Ge multilayers. *Physical Review B*, 52(5):3795–3801, 8 1995.

[50] Alice E. White, K. T. Short, R. C. Dynes, A. F. J. Levi, M. Anzlowar, K. W. Baldwin, P. A. Polakos, T. A. Fulton, and L. N. Dunkleberger. Controllable reduction of critical currents in YBa2Cu3O7δ films. *Applied Physics Letters*, 53(11):1010, 1988.

[51] J. M. Valles, A. E. White, K. T. Short, R. C. Dynes, J. P. Garno, A. F. J. Levi, M. Anzlowar, and K. Baldwin. Ion-beam-induced metal-insulator transition in Y Ba 2 Cu 3 O 7 δ : A mobility edge. *Physical Review B*, 39(16):11599–11602, 6 1989.

[52] Wolfgang Lang and Johannes D. Pedarnig. Ion Irradiation of High-Temperature Superconductors and Its Application for Nanopatterning. pages 81–104. Springer Berlin Heidelberg, 2010.

[53] James F. Ziegler, M.D. Ziegler, and J.P. Biersack. SRIM The stopping and range of ions in matter (2010). *Nuclear Instruments and Methods in Physics Research Section B: Beam Interactions with Materials and Atoms*, 268(11):1818–1823, 2010.

[54] AF Andreev. Thermal conductivity of the intermediate state of superconductors, ii. *Sov. Phys. JETP*, 20:1490, 1965.

[55] G. E. Blonder, M. Tinkham, and T. M. Klapwijk. Transition from metallic to tunneling regimes in superconducting microconstrictions: Excess current, charge imbalance, and supercurrent conversion. *Physical Review B*, 25(7):4515–4532, 4 1982.

[56] M. Octavio, M. Tinkham, G. E. Blonder, and T. M. Klapwijk. Subharmonic energy-gap structure in superconducting constrictions. *Physical Review B*, 27(11):6739–6746, 6 1983.

[57] S.A. Cybart, K. Chen, and R.C. Dynes. Planar $rm YBa_2rm Cu_3rm O_7-delta$ Ion Damage Josephson Junctions and Arrays. *IEEE Transactions on Appiled Superconductivity*, 15(2):241–244, 6 2005.

[58] S.A. Cybart, E.Y. Cho, T.J. Wong, V.N. Glyantsev, J.U. Huh, C.S. Yung, B.H. Moeckly, J.W. Beeman, E. Ulin-Avila, S.M. Wu, and R.C. Dynes. Large voltage modulation in magnetic field sensors from two-dimensional arrays of Y-Ba-Cu-O nano Josephson junctions. *Applied Physics Letters*, 104(6), 2014.

[59] Shinji Matsui and Yukinori Ochiai. Focused ion beam applications to solid state devices. *Nanotechnology*, 7(3):247–258, 9 1996.

[60] R. W. Moseley, W. E. Booij, E. J. Tarte, and M. G. Blamire. Direct writing of low T[sub c] superconductor-normal metal-superconductor junctions using a focused ion beam. *Applied Physics Letters*, 75(2):262, 1999.

[61] C H Wu, Y T Chou, W C Kuo, J H Chen, L M Wang, J C Chen, K L Chen, U C Sou, H C Yang, and J T Jeng. Fabrication and characterization of high-T(c)YBa(2)Cu(3)O(7-x) nanoSQUIDs madeby focused ion beam milling. *Nanotechnology*, 19(31):315304, 8 2008.

[62] C.-H. Chen, Z. Trajanovic, Z. W. Dong, C. J. Lobb, T. Venkatesan, K. Edinger, J. Orloff, and J. Melngailis. Fabrication of high-temperature superconductor Josephson junctions by focused ion beam milling. *Journal of Vacuum Science & Technology B: Microelectronics and Nanometer Structures*, 15(6):2379, 11 1997.

[63] M. J. Zani, J. A. Luine, R. W. Simon, and R. A. Davidheiser. Focused ion beam high Tc superconductor dc SQUIDs. *Applied Physics Letters*, 59(2):234, 1991.

[64] B. W. Ward, John A. Notte, and N. P. Economou. Helium ion microscope: A new tool for nanoscale microscopy and metrology. *Journal of Vacuum Science & Technology B: Microelectronics and Nanometer Structures*, 24(6):2871, 2006.

[65] I. Iguchi and Z. Wen. Tunnel gap structure and tunneling model of the anisotropic YBaCuO/I/Pb junctions. *Physica C: Superconductivity*, 178(1-3):1–10, 7 1991.

[66] H. L. Edwards, J. T. Markert, and A. L. de Lozanne. Energy gap and surface structure of YBa 2 Cu 3 O 7 x probed by scanning tunneling microscopy. *Physical Review Letters*, 69(20):2967–2970, 11 1992.

[67] Hikari Kimura, R. P. Barber, S. Ono, Yoichi Ando, and R. C. Dynes. Scanning Josephson Tunneling Microscopy of Single-Crystal Bi 2 Sr 2 CaCu 2 O 8 + δ with a Conventional Superconducting Tip. *Physical Review Letters*, 101(3):037002, 7 2008.

[68] Hikari Kimura, R. P. Barber, S. Ono, Yoichi Ando, and R. C. Dynes. Josephson scanning tunneling microscopy: A local and direct probe of the superconducting order parameter. *Physical Review B*, 80(14):144506, 10 2009.

[69] S. Nawaz, R. Arpaia, F. Lombardi, and T. Bauch. Microwave Response of Superconducting Y Ba 2 Cu 3 O 7 δ Nanowire Bridges Sustaining the Critical Depairing Current: Evidence of Josephson-like Behavior. *Physical Review Letters*, 110(16):167004, 4 2013.

[70] Peter A Rosenthal, M R Beasley, K Char, M S Colclough, and G Zaharchuk. Flux focusing effects in planar thin-film grain-boundary Josephson junctions. *Applied physics letters*, 59(26):3482–3484, 1991.

[71] C. C. Tsuei, J. R. Kirtley, C. C. Chi, Lock See Yu-Jahnes, A. Gupta, T. Shaw, J. Z. Sun, and M. B. Ketchen. Pairing Symmetry and Flux Quantization in a Tricrystal Superconducting Ring of Y Ba 2 Cu 3 O 7 δ. *Physical Review Letters*, 73(4):593–596, 7 1994.

[72] C. C. Tsuei and J. R. Kirtley. Pairing symmetry in cuprate superconductors. *Reviews of Modern Physics*, 72(4):969–1016, 10 2000.

[73] J. R. Kirtley, C. C. Tsuei, A. Ariando, C. J. M. Verwijs, S. Harkema, and H. Hilgenkamp. Angle-resolved phase-sensitive determination of the in-plane gap symmetry in YBa2Cu3O7δ. *Nature Physics*, 2(3):190–194, 3 2006.

[74] D. J. Van Harlingen. Phase-sensitive tests of the symmetry of the pairing state in the high-temperature superconductorsEvidence for d x 2 y 2 symmetry. *Reviews of Modern Physics*, 67(2):515–535, 4 1995.

[75] R. Kleiner, A. S. Katz, A. G. Sun, R. Summer, D. A. Gajewski, S. H. Han, S. I. Woods, E. Dantsker, B. Chen, K. Char, M. B. Maple, R. C. Dynes, and John Clarke. Pair Tunneling from ¡i¿c¡/i¿ -Axis YBa 2 Cu 3 O 7 x to Pb: Evidence for ¡i¿s¡/i¿ -Wave Component from Microwave Induced Steps. *Physical Review Letters*, 76(12):2161–2164, 3 1996.

[76] K. A. Kouznetsov, A. G. Sun, B. Chen, A. S. Katz, S. R. Bahcall, John Clarke, R. C. Dynes, D. A. Gajewski, S. H. Han, M. B. Maple, J. Giapintzakis, J.-T. Kim, and D. M. Ginsberg. c -axis Josephson Tunneling between YBa 2 Cu 3 O 7 δ and Pb: Direct Evidence for Mixed Order Parameter Symmetry in a High-T c Superconductor. *Physical Review Letters*, 79(16):3050–3053, 10 1997.

[77] K. Kitazawa, M. Nantoh, S. Heike, A. Takagi, H. Ikuta, and T. Hasegawa. Superconducting gap observed by the atomic-site tunneling spectroscopy on YBCO and BSCCO. *Physica C: Superconductivity*, 209(1-3):23–26, 4 1993.

[78] Claudia D. Tesche and John Clarke. dc SQUID: Noise and optimization. *Journal of Low Temperature Physics*, 29(3-4):301–331, 11 1977.

[79] D. Koelle, R. Kleiner, F. Ludwig, E. Dantsker, and John Clarke. High-transition-temperature superconducting quantum interference devices. *Reviews of Modern Physics*, 71(3):631–686, 4 1999.

[80] R. C. Jaklevic, John Lambe, A. H. Silver, and J. E. Mercereau. Quantum Interference Effects in Josephson Tunneling. *Physical Review Letters*, 12(7):159–160, 2 1964.

[81] M. I. Faley, U. Poppe, R. E. Dunin-Borkowski, M. Schiek, F. Boers, H. Chocholacs, J. Dammers, E. Eich, N. J. Shah, A. B. Ermakov, V. Y. Slobodchikov, Y. V. Maslennikov, and V. P. Koshelets. High-t_C dc squids for magnetoencephalography. *IEEE Transactions on Applied Superconductivity*, 23(3):1600705–1600705, June 2013.

[82] M.I. Faley, U. Poppe, K. Urban, D.N. Paulson, T.N. Starr, and R.L. Fagaly. Low noise HTS dc-SQUID flip-chip magnetometers and gradiometers. *IEEE Transactions on Appiled Superconductivity*, 11(1):1383–1386, 3 2001.

[83] R.P. Giffard. Flux locked loop, January 18 1977. US Patent 4,004,217.

[84] John Clarke and Alex I Braginski. The squid handbook. 2004.

[85] C P Foley, H Hilgenkamp, Voss R F Laibowitz R B Ketchen M B Broers A N Hahlohm H D Lubbig H, Hilgenkamp H Vulink B Veldhuis D Blank D H A, Booij W, Rogalla H, de Muijnck H Pedyash M V, Blank D H A, Rogalla H, Kopley T Ketchen M B, Ling H, Davies J Hao L Gallop J, Joseph-Franks P W, Macfarlane J, Mailly D Barbara B Benoit A Thomas L Wernsdorfer W, Hasselbach K, Suran G, Lam S K H L, Tilbrook D, Anderson P W H, Dayem A, Bouchiat V Ondarcuhu T Cleuziou J-P, Wernsdorfer W, Monthioux M, Tettamanzi G C Pakes C I Potenza A Marrows C H Prawer S Jamieson D N, Gallop J C Cox D Beyer J Drung D Hao L, Macfarlane J C, Schurig T, Borger B Pleikies J Veldhuis D Troeman A G R, Derking H, Hilgenkamp H, Bert J A Hicks C W Large J Edwards H Koshnick N C, Huber M E, Moler K A, Kuo W C Chen J H Wang L M Chen J C Chen K L Sou U C Yang H C Wu C H, Chou Y T, Jeng J T, Wang J Mensah S L, Prasad A, Yap Y K, Bakkers E P A M De Franceschi S van Dam J A, Nazarov Y V, Kouwenhoven L P, Thirion C Wernsdorfer W Fouernier T Bouchiat V, Faucher M, Pannetier B, Fruchart O Wernsdorfer W Faucher M, Jubert P O, Bouchiat V, Neel L, Neel L, Bernstein E Depuis V Tournier T Crozes T Bonet E Raufast C, Tamion A, Wernsdorfer W, Wiogo H T R Lam S K H, Yang W, Foley C P, Ramelow S Cimmino A Jamieson D N Pakes C I, George D P, Pawer S, Amro N A Cruchon-Dupeyrat S Chen S Garno J C, Yang Y, Lui G Y, Vohralik P F H, Lam S K, Tilbrook D L, Pegrum C, Vijay R Fathalizaden A Siddiqi I Hatridge M Clark J, Lam S H K Foley C P Josephs-Franks P Hao L, Macfarlane J C, Gallop J C, Hao L et al, Ullom J N et al, Lam S H K, Lam S K H, Kirtely J Carlsen A Chen J Troeman A-Hilgenkamp H Freitag M, Tsang J C, Avouris P, Stawiasz K G sun J Z Gallagher W J Blanton S H Kirtley J R, Ketchen M B, Wind S J, Troeman A G P, Levy J Meier F, Loss D, del Barco E Hernandez J M Tejada J, Chudnoivsky E M, Spiller T P, Watson A, Gallop J C, Gallop J C Cox D Hutson D Josephs-Franks P Chen J Hao L, Macfarlane J C, and Lam S K H. Why NanoSQUIDs are important: an introduction to the focus issue. *Superconductor Science and Technology*, 22(6):064001, 6 2009.

[86] S. Berggren, G. Prokopenko, P. Longhini, A. Palacios, O.A. Mukhanov, A. Leese De Escobar, B.J. Taylor, M.C. De Andrade, M. Nisenoff, R.L. Fagaly, T. Wong, E. Cho, E. Wong, and V. In. Development of 2-D Bi-SQUID arrays with high linearity. *IEEE Transactions on Applied Superconductivity*, 23(3), 2013.

[87] S Basavaiah and RF Broom. Characteristics of in-line josephson tunneling gates. *IEEE Transactions on Magnetics*, (2):759–762, 1975.

[88] Travis J. Wong. *Arrays of Superconducting Quantum Interference Devices (SQUIDs) In Y-Ba-Cu-O Utilizing Ion Irradiation Patterning*. PhD thesis, University of California, San Diego, 9500 Gilman Dr. La Jolla, CA 92093 USA, 2016.

[89] C. P. Bean. Magnetization of Hard Superconductors. *Physical Review Letters*, 8(6):250–253, 3 1962.

[90] Y. B. Kim, C. F. Hempstead, and A. R. Strnad. Magnetization and Critical Supercurrents. *Physical Review*, 129(2):528–535, 1 1963.